Dynamic analysis of viscoelastic floating membranes using monolithic Finite Element method

Agarwal, Shagun; Colomés, Oriol; Metrikine, Andrei V.

DOI
10.1016/j.jfluidstructs.2024.104167

Publication date
2024

Document Version
Final published version

Published in
Journal of Fluids and Structures

Journal of Fluids and Structures 129 (2024) 104167

Contents lists available at ScienceDirect

Journal of Fluids and Structures

journal homepage: www.elsevier.com/locate/jfs

Dynamic analysis of viscoelastic floating membranes using monolithic Finite Element method

Shagun Agarwal *, Oriol Colomés, Andrei V. Metrikine

Faculty of Civil Engineering and Geosciences, Delft University of Technology, The Netherlands

ARTICLE INFO

Keywords:
Floating membrane
Fluid–structure interaction
Monolithic FEM
Floating solar
Hydroelasticity
Wet modes

ABSTRACT

The paper presents a monolithic finite element model for the hydro-visco-elastic analysis of floating membranes interacting with ocean waves. The formulation couples linearised potential flow and viscoelastic membrane equations, offering a versatile tool for modelling arbitrarily shaped floating membranes in varying sea-bed topography. The paper also presents a wet modal analysis for the coupled problem, accounting for the added mass and stiffness of the surrounding fluid. This model is used to study the dependence of the wet natural frequencies of floating membranes on the material properties. It is also used to analyse the reflection, transmission, scattering and absorption of ocean wave energy by 1D and 2D floating membranes. Notably, the paper underscores the impact of proportional material damping on these observed phenomena. The results highlight local peaks in the viscoelastic behaviour at the calculated wet natural frequencies, and demonstrate the outward dispersion of incoming wave around finite 2D membranes. Furthermore, the model is employed to examine the interaction of viscoelastic membranes with other structures, such as a monopile, under the influence of ocean waves. This comprehensive investigation contributes to a deeper understanding of the fluid–structure interaction inherent to certain floating solar, wave-energy converter and floating breakwater technologies.

1. Introduction

Floating membranes are flexible structures made of materials such as reinforced rubber, geotextile fibres or plastics that are widely used in offshore and coastal engineering applications. One of the most common applications are floating breakwaters, either vertical, e.g. Williams (1996), or horizontal, e.g. Cho and Kim (1998). The use of floating membranes as floating breakwaters presents several advantages: they are lightweight, easily deployable, reusable and have minimum impact on key coastal processes such as sediment transport and fish migration.

The use of floating membranes is not limited to breakwater applications. Several innovative technologies are adopting these as compliant support structures. Most crucial among these is the floating photovoltaic systems (FPVs) (Cazzaniga and Rosa-Clot, 2021; Vo et al., 2021). FPVs are a cutting-edge new technology aimed at revolutionising ocean renewables by deploying solar platforms in lakes, coastal and offshore waters. This technology has several benefits, including improved efficiency driven by convective cooling from the surrounding water, undisturbed access to solar irradiance and critically, avoiding use of the depleting and valuable land resource. FPVs can also explore synergy with offshore wind farms by deploying these platforms in the exclusion zones of offshore wind turbines, thus enabling multi-modal energy production. Here several prototypes, such as *Ocean Sun's OS-50* (Ocean Sun, n.d.) have explored the possibility of using crystalline or amorphous panels on top of floating membranes. This design has the

* Corresponding author.
E-mail addresses: s.agarwal@tudelft.nl (S. Agarwal), j.o.colomesgene@tudelft.nl (O. Colomés), a.metrikine@tudelft.nl (A.V. Metrikine).

https://doi.org/10.1016/j.jfluidstructs.2024.104167
Received 22 December 2023; Received in revised form 30 May 2024; Accepted 9 July 2024
Available online 23 July 2024

distinct advantage of easy deployment, low cost and excellent serviceability. However, the interaction of these large platforms with ocean waves and their resulting structural resilience in harsh offshore conditions is presently an active field of research, primarily focusing on the interaction of floating beams with ocean waves using analytical (Xu and Wellens, 2022), semi-analytical (Sree et al., 2021) and numerical (Sree et al., 2022) approaches. Another set of applications gaining attention in recent years is the use of flexible membranes as wave energy converters (Michele et al., 2020; Collins et al., 2021; Boren, 2021). These systems aim at converting the ocean wave energy to motion of large floating platforms, and thereby harvest energy through viscoelastic membranes, power-take-off systems or damped mooring systems. Here several prototypes explore the use of piezoelectric (Kargar and Hao, 2022) and dielectric (Moretti et al., 2022) materials for embedding the energy harvesting mechanism within floating membranes, resulting in a continuous energy extraction mechanism. The primary advantage of this approach lies in its ability to harvest energy from a broad range of ocean wave frequencies, leading to increased operational bandwidth and efficiency. However, the successful implementation of this concept requires an improved understanding of the inherent fluid–structure interaction (FSI) between ocean waves and viscoelastic *Very Large Floating Structures* (VLFS). The use of flexible floating membranes in these wide ranges of applications highlights the need for efficient and versatile methods and tools for their design and analysis, especially when considering the effect of waves in offshore environments.

Traditionally, the analysis of Very Large Floating Structures (VLFS) has been conducted under the assumption of thin-plate theory. A comprehensive review of literature focusing on the hydro-elastic response of pontoon-type VLFS, assuming thin plate theory, is provided in Watanabe et al. (2004), Ohmatsu (2005), Lamas-Pardo et al. (2015) and Zhang and Schreier (2022). In the frequency domain, solution approaches are typically classified into modal expansion methods and direct methods. The modal expansion method involves decomposing the dynamic response using vibration modes of the plate. Often, these vibration modes are the dry modes (Kashiwagi, 1998; Taylor and Ohkusu, 2000), although certain studies also consider the wet modes of the plate (Humamoto and Fujita, 2002; Loukogeorgaki et al., 2012), accounting for the added mass resulting from the inertia of the surrounding water. On the other hand, the direct method solves the hydro-elastic governing equation without the use of eigen modes (Colomés et al., 2022). While there is ample literature on the hydro-elastic response of thin-plate pontoon-type VLFS, there is limited literature on the hydro-elastic response of VLFS constructed from pre-tensioned membranes. The structural response of pre-tensioned membranes differs from that of thin plates. In thin plates, the transverse restoring force is primarily governed by the bending stiffness of the plate. In contrast, in pre-tensioned membranes, the transverse restoring force is dominated by the axial pre-tension in the membrane. This assertion is supported by a dimensional analysis presented in Section 2.2.1 of this paper. Therefore, the focus of this paper is to address this gap in the literature and study the hydro-elastic response of pre-tensioned floating membranes.

The study of hydro-elastic phenomena in floating membranes faces various challenges, namely: a strong interaction between elastic deformation and the response to hydrodynamic forces, a high dependency of the response on the material properties and membrane pre-tension, the characterisation of the response of finite dimensional structures interacting with nonlinear waves, or the nonlinearities inherent to fluid–structure interaction (FSI). Conventionally, floating membranes have been studied as vertical breakwaters, which restrict the horizontal flux of wave energy. These analyses focus largely on their performance in reflecting incoming waves. These include experimental studies using single screen (Kim and Kee, 1996), and a number of analytical studies on single screen and dual screen wave barriers (Lo, 2000; Suresh Kumar et al., 2007). On the other hand, horizontally floating membranes suppress vertical fluid motion, thus resulting in partial reflection and significant scattering of the incoming wave. Some studies have employed experimental analysis of flexible floating membranes (Schreier and Jacobi, 2021), but they have limitations regarding structural size and wave conditions. Horizontal floating membranes have been analysed by analytical studies using simplified mode expansion and boundary integral techniques for floating and submerged membranes in infinite depths, finite depths and stepped sea-bed profiles (Karmakar and Sahoo, 2008). Several studies have also expanded this approach to porous membranes (Koley and Sahoo, 2017; Guo et al., 2022) by modifying the kinematic boundary condition based on Darcy's law. Similar approach was implemented in Mohapatra and Guedes Soares (2022) for studying interaction of floating and porous submerged flexible tensioned plate with linear waves. However, these approaches are often limited to regular sea-bed topographies and regular shaped or semi-infinite membranes. This limits the understanding of the multi-directional scattering of ocean waves by finite, irregularly shaped, an-isotropic membranes. Additionally, these approaches are largely limited to linear analysis. Hence there is a need to develop solutions for arbitrarily shaped membranes in variable bathymetry.

The numerical solution to this problem can be envisioned in several ways. There are two main considerations: one-way or two-way interaction, and partitioned or monolithic approach. A one-way interaction only considers the influence of waves on the structural deformation of the membrane, and completely disregards the dispersion and dissipation of waves of the floating membrane. This basic approach is only valid for floating islands with characteristic lengths much smaller than the ocean waves. Nonetheless, the approach has been used to estimate the interaction of *Ocean Sun's OS-50* platform in Berstad and Grøn (2023). A two-way interaction considers the transformation of the waves by the structure, along with the structural deformation. For VLFS, this two-way interaction is inevitable and critical due to the scale of the problem, resulting in partial reflection, outward/inward dispersion of the waves, along with the structural deformation (Zhang and Schreier, 2022). This two-way interaction can be implemented using a partitioned or a monolithic approach. A partitioned approach would solve the membrane and the fluid problems using two separate models, and enforce the interaction through iterative algorithms. This approach allows the use of best off-the-shelf models for each problem, but it often leads to slow simulations and strict stability requirements, limiting their practical application. Recently, Ma et al. (2020) studied the hydro-elastic behaviour of a thin-elastic floating plate using a partitioned approach by coupling smoother particle hydrodynamics (SPH) for fluids with finite-element method (FEM) for structural deformation. Alternatively, a monolithic approach formulates a single system of coupled equations for the fluid and the solid, with improved numerical

stability, strong coupling and simultaneous solution of the multi-physics problem. The monolithic approach often leads to a mixed-dimension system of partial differential equations, often requiring custom models. However, here the finite-element method (FEM) is particularly suitable in modelling the multi-dimensional multi-physics system. This was demonstrated in the recent work (Colomés et al., 2022), where a monolithic framework coupling potential flow with Kirchhoff plate theory was presented using a state-of-the-art FEM library *Gridap* (Badia and Verdugo, 2020). The work demonstrated the capabilities of such a monolithic model in studying the interaction of arbitrarily shaped floating plates with ocean waves. The current literature lacks a similar model for floating membranes. Additionally, a monolithic approach facilitates the development of a wet modal analysis for the floating membrane, taking into account the added mass caused by the acceleration of the surrounding fluid and the hydrostatic-gravitational stiffness. The presence of fluid can notably alter the natural frequency of the membrane. This phenomenon was explored in Loukogeorgaki et al. (2012), focusing on a floating flexible mat and highlighting the consequences of natural frequency on the performance of the mat as a breakwater. A similar investigation for floating membranes is essential for identifying the predominant natural frequencies and modes of the membrane, as well as understanding their impact on the membrane's performance as a wave barrier or wave-absorber.

Finally, a comprehensive description of a floating membrane is incomplete, without addressing its material damping. Besides exhibiting elastic behaviour due to structural deformation, a membrane often demonstrates dissipative behaviour attributed to material damping. This gives rise to a hydro-viscoelastic, or simply *viscoelastic*, interaction between the floating membrane and the ocean waves, resulting in deformation and viscous dissipation within this membrane. Such a viscoelastic material is more representative of the real floating membrane-type breakwater or FPV platforms, where the material damping can play a crucial role in scattering and dissipating the incoming wave energy. Additionally, this material damping can also represent the wave energy extracted by a floating membrane-type wave-energy converter, especially when the extraction mechanism is from the use of dielectric or piezoelectric designs throughout the membrane (Boren, 2021). This extracted energy hence represents the capture width of such a wave energy converter, and therefore is crucial in estimating the performance and survival of such a system in the offshore environment. Recently analysis by Trivedi and Koley (2022) studied the performance of 1D viscoelastic membrane as a wave-barrier in constant water-depth using the boundary element method. However, the contemporary literature lacks studies on 2D finite viscoelastic membranes and their interaction with other bodies.

This manuscript addresses these gaps by presenting a monolithic FEM model for viscoelastic analysis of 2D finite pre-tensioned floating membranes, with arbitrary shapes and in variable bathymetry. Specifically, the developments in this manuscript include (a) monolithic finite-element formulation for the multi-physics problem involving linear viscoelastic pre-tensioned membrane and linearised potential flow, (b) wet modal analysis of the coupled problem, accounting for the influence the surrounding fluid. The formulation builds upon the FEM approach proposed by Akkerman et al. (2020) for potential flow with linearised free-surface boundary conditions, and its extension to floating beam by Colomés et al. (2022). Subsequently, the manuscript employs this model to investigate viscoelastic interactions, specifically: (a) examining the dependence of the wet natural frequencies on the material properties of the membrane, (b) reflection and transmission of surface waves by the viscoelastic membrane, (c) scattering of the waves by 2D finite floating membranes, (d) estimating drift force and wave energy absorbed (or dissipated) by the viscoelastic membrane, and finally (e) interaction of the viscoelastic membrane with a monopile foundation. The analysis in this manuscript is limited to the linearised problem. Nevertheless, it establishes the basis for extension to the nonlinear problem in our future work.

The manuscript is organised as follows. Section 2 presents the governing equations for the fluid and the structural problem, along with the coupling boundary condition. In Section 3 we develop the monolithic numerical formulation for the VLFS floating membrane, describing the discretised problem and proving the consistency and energy conservation properties of the discrete form. Section 4 presents the wet modal analysis, developed using the weak-form of the coupled problem and the associated iterative algorithm for calculating the wet natural frequency of the system. Section 5 presents a range of numerical studies, investigating the aforementioned viscoelastic behaviour of 1D and 2D floating membranes, with final conclusions drawn in Section 6.

2. Problem setting

The problem is defined in a Cartesian coordinate system, consisting of a 3D fluid domain Ω. The Z-axis is assumed to be vertically upwards. It is bounded by irregular bottom surface Γ_b, inlet and outlet surfaces Γ_{in} and Γ_{out}, respectively, and the fluid free-surface Γ_{fs}. Additionally, the 3D fluid domain is bounded by a 2D thin floating membrane, denoted by Γ_m. The boundaries of Γ_m are denoted by Λ_1 and Λ_2. Fig. 1a highlights these surfaces in the schematic for the boundary value problem. The analysis in this manuscript considers the following assumptions:

- **Assumption 1** The flow within Ω is incompressible, inviscid and irrotational, and the free-surface elevation is assumed to be small compared to the wave-length and the water-depth. Therefore, the fluid domain is described by the linearised potential flow theory.
- **Assumption 2** Absence of air gap (cavitation) between the fluid free-surface and the floating membrane.
- **Assumption 3** Thin homogeneous membrane with small transverse deflection and no significant surge displacement.

The present manuscript does not consider the non-linearity associated with ocean waves and membrane deflection.

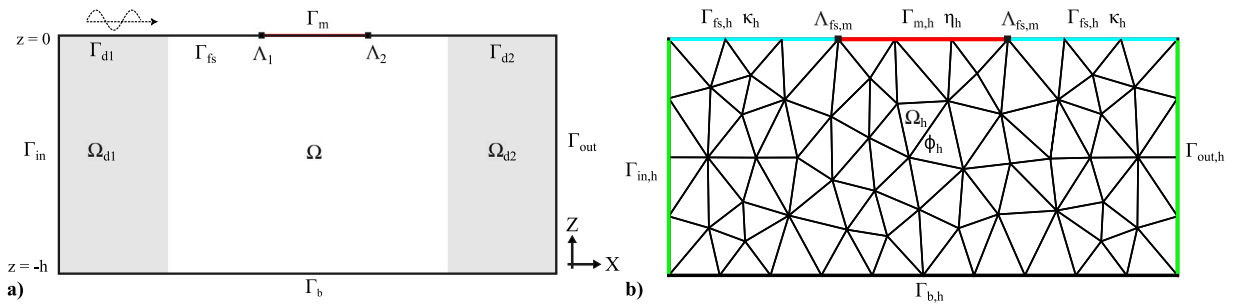

Fig. 1. (a) Schematic of the boundary value problem. (b) Schematic of the discretised boundary value problem. Note that the membrane $\Gamma_{m,h}$ is a portion of the boundary of the discretised fluid domain Ω_h.

2.1. Linear potential flow theory

For the irrotational and inviscid flow with the velocity vector $\mathbf{u}$ in the fluid domain Ω, there exists a scalar potential field ϕ, such that $\mathbf{u} = \nabla\phi$. Further, the incompressible flow assumption implies $\nabla \cdot \mathbf{u} = 0$, thus returning the following fluid flow governing equation Eq. (1).

$$\Delta\phi = 0 \qquad \text{in } \Omega. \tag{1}$$

The governing equation is supplemented by the kinematic and dynamic conditions on the domain boundaries, which are written as follows.

$$\mathbf{n} \cdot \nabla\phi = 0 \qquad \text{on } \Gamma_b \tag{2a}$$

$$\mathbf{n} \cdot \nabla\phi = u_{in} \qquad \text{on } \Gamma_{in} \tag{2b}$$

$$\mathbf{n} \cdot \nabla\phi = u_{out} \qquad \text{on } \Gamma_{out} \tag{2c}$$

$$\mathbf{n} \cdot \nabla\phi = \kappa_t \qquad \text{on } \Gamma_{fs} \tag{2d}$$

The kinematic condition Eq. (2a) implies no-penetration through the bottom boundary Γ_b, while Eqs. (2b) and (2c) control the inflow and outflow across Γ_{in} and Γ_{out}, respectively. Here $\mathbf{n}$ is the outward unit normal to the domain boundary. The kinematic free-surface condition (KFSC) relates the free-surface elevation κ with the flow velocity, assuming no-flow across the moving free-surface. For the present analysis, this condition is linearised given in Eq. (2d).

$$p = -\rho\phi_t - \rho g\kappa - \frac{1}{2}\rho(\nabla\phi)^2 \simeq -\rho\phi_t - \rho g\kappa \tag{3a}$$

$$\phi_t = -g\kappa \qquad \text{on } \Gamma_{fs} \tag{3b}$$

The pressure at the free-surface is given by the linearised Bernoulli equation, Eq. (3a). Here, ρ is the fluid density and $g = 9.81\ \text{ms}^{-2}$ is the acceleration due to gravity. For the free-surface Γ_{fs} exposed to the atmosphere, $p = p_{atm} = 0$, resulting in the dynamic free-surface boundary condition (DFSC), Eq. (3b).

2.2. Viscoelastic membrane

This paper presents the analysis for 2D viscoelastic membrane floating on the free-surface of fluid in 3D domain. In order to set up the governing equations of the membrane, we first need to understand the relative dominance of the axial tensioning and the bending stiffness for such a membrane.

2.2.1. Dimensional analysis of tensioned beam

We conduct an order of magnitude analysis using a 1D solid tensioned beam, having a length L_m and thickness h_m, made of material with Young's modulous E and density ρ_m. The structural governing equation for this tensioned beam is as follows.

$$\rho_m h_m \eta_{tt} - T\eta_{xx} + EI\eta_{xxxx} = p_m \tag{4}$$

Here η is the transverse deflection, p_m is the transverse load, $I = \frac{1}{12}h_m^3$ is the moment of inertia per unit width for the beam, assuming a solid cross-section, and $T = E\epsilon h_m$ is the axial pre-tension per unit width in the beam, with initial axial strain ϵ. Hence the term $-T\eta_{xx}$ is the transverse restoring force due to the pre-tensioning of the beam and $EI\eta_{xxxx}$ is the transverse restoring force due to the bending stiffness of the beam.

Consider the non-dimensional quantities $\tilde{\eta} = \eta/h_m$, $\tilde{x} = x/L_m$ and $\tilde{t} = \omega t$, where ω is the excitation wave frequency. The non-dimensional form of the governing Eq. (4) is given as follows.

$$\rho_m h_m^2 \omega^2 \tilde{\eta}_{\tilde{t}\tilde{t}} - \frac{E\epsilon\, h_m^2}{L_m^2} \tilde{\eta}_{\tilde{x}\tilde{x}} + \frac{E\, h_m^4}{12\, L_m^4} \tilde{\eta}_{\tilde{x}\tilde{x}\tilde{x}\tilde{x}} = p_m \tag{5a}$$

$$\implies \tilde{\eta}_{\tilde{t}\tilde{t}} - \frac{E\epsilon}{\rho_m \omega^2 L_m^2} \tilde{\eta}_{\tilde{x}\tilde{x}} + \frac{E\, h_m^2}{12\, \rho_m \omega^2\, L_m^4} \tilde{\eta}_{\tilde{x}\tilde{x}\tilde{x}\tilde{x}} = \frac{p_m}{\rho_m h_m^2 \omega^2} \tag{5b}$$

$$\implies \tilde{\eta}_{\tilde{t}\tilde{t}} - \beta\, \tilde{\eta}_{\tilde{x}\tilde{x}} + \chi\, \beta\, \tilde{\eta}_{\tilde{x}\tilde{x}\tilde{x}\tilde{x}} = \frac{p_m}{\rho_m h_m^2 \omega^2} \qquad \text{where } \beta = \frac{E\epsilon}{\rho_m \omega^2 L_m^2}, \quad \chi = \frac{1}{12} \frac{h_m^2}{L_m^2} \frac{1}{\epsilon} \tag{5c}$$

From Eq. (5c), we note that χ is the ratio of transverse restoring force due to the bending stiffness vs pre-tensioning. Hence if $\chi \ll 1$ then the pre-tensioning would dominate, and if $\chi \gg 1$ then the bending stiffness would dominate. VLFS are typically thin structures, having ratio $\frac{h_m}{L_m} \ll 1$. However, in most cases, the VLFS structures do not have significant pre-tensioning, i.e, $\epsilon \to 0$. In these cases, $\lim_{\epsilon \to 0} \chi \gg 1$, and hence it is crucial to consider the bending stiffness, while the pre-tensioning can be neglected.

In this manuscript, we are studying pre-tensioned membranes. Such structures typically have very small thickness, i.e., $\frac{h_m}{L_m} \lll 1$ and are pre-tensioned using significant initial axial strain, i.e., $\epsilon \neq 0$. For these structures, $\chi \lll 1$, and hence the bending stiffness can be neglected. Therefore, moving forward, we will not consider the bending stiffness of the floating membrane in this manuscript.

Additionally, the practical implementation of this pre-tensioning can be achieved through various methods. For instance, in a floating membrane platform with a free edge, pre-tensioning can be accomplished using an outer floating ring. For a floating membrane platform with a fixed edge, pre-tensioning can be achieved by utilising mooring lines attached to floater buoys.

2.2.2. Governing equation for viscoelastic membrane

As shown in Section 2.2.1, a thin elastic pre-tensioned floating membrane can be considered as a limiting case of a tensioned beam plate, with bending stiffness approaching zero. The governing equation for transverse deflection η of a materially damped, pre-tensioned, thin and homogeneous 2D membrane, due to the action of transverse load p_m can hence be obtained by modifying Eq. (4) as the following (Guo et al., 2022).

$$p_m = m\eta_{tt} - \nabla_h \cdot \left(T\, \nabla_h \eta\right) - \nabla_h \cdot \left(\tau T\, \nabla_h \eta_t\right) \qquad \text{where } \nabla_h = \frac{\partial}{\partial x}\, \hat{\imath} + \frac{\partial}{\partial y}\, \hat{\jmath} \tag{6}$$

Once again, in this equation, the parameter $m = \rho_m h_m$ represents the mass per unit area of the membrane, with ρ_m and h_m denoting the density and thickness of the membrane, respectively. The variable T corresponds to the pre-tension in the stretched membrane. The material damping is assumed to be directly proportional to the membrane's stiffness, with the proportionality constant being the damping coefficient τ (Trivedi and Koley, 2022). In this manuscript, we only consider an isotropic membrane with uniform pre-tension T and uniform viscous damping coefficient τ. However, the presented numerical model can be applied to an anisotropic membrane problem with m, T and τ varying over the membrane. The boundary conditions for membrane edges Λ_1, Λ_2 for fixed and free edge conditions are given by the following Eq. (7).

$$\eta = 0 \qquad \text{(fixed edge)} \tag{7a}$$

$$\nabla_h(\eta) \cdot \mathbf{n} = 0 \qquad \text{(free-edge)} \tag{7b}$$

In this equation, $\mathbf{n}$ is the outward unit-normal at the membrane boundaries.

2.3. Coupling boundary condition

The fluid free-surface under the membrane will track along the deflection of the membrane, considering assumptions 2 and 3. Hence, the kinematic free-surface boundary condition on Γ_m is obtained by equating η_t with normal velocity $\mathbf{n} \cdot \nabla\phi$; and the dynamic free-surface boundary conditions for Γ_m is obtained by equating the transverse load p_m in the membrane from Eq. (6), with the free-surface pressure p from equation Eq. (3a). The resultant coupling boundary conditions at the membrane-fluid interface are given by Eq. (8).

$$\mathbf{n} \cdot \nabla\phi = \eta_t \qquad \text{on } \Gamma_m \tag{8a}$$

$$m_\rho \eta_{tt} - \nabla_h \cdot (T_\rho\, \nabla_h \eta) - \nabla_h \cdot (\tau T_\rho\, \nabla_h \eta_t) + \phi_t + g\eta = 0 \qquad \text{on } \Gamma_m \tag{8b}$$

Here, $m_\rho = m/\rho$ is the submerged draft of the membrane, while $T_\rho = T/\rho$. This completes the formulation of the mixed-dimension boundary value problem with the 2D governing equation Eq. (1), with boundary conditions Eqs. (2), (3b) and (8) for the fluid domain, and the boundary condition Eq. (7) for the membrane edges.

2.4. Frequency domain formulation

Assuming separation of variables and steady-state, the solution for ϕ, η, κ can be written as complex expressions $\phi(x,z,t) = \bar{\phi}(x,z)\exp(-i\omega t)$, $\eta(x,t) = \bar{\eta}(x)\exp(-i\omega t)$ and $\kappa(x,t) = \bar{\kappa}(x)\exp(-i\omega t)$. The resulting linearised governing equation and the associated boundary conditions fluid and membrane can therefore be reduced to Eq. (9). In order to simplify the notation, we neglect the over-bar hereafter.

$$\Delta\phi = 0 \qquad \text{in } \Omega \tag{9a}$$

$$\phi_z + i\omega\kappa = 0 \qquad \text{on } \Gamma_{fs} \tag{9b}$$

$$\phi_z + i\omega\eta = 0 \qquad \text{on } \Gamma_m \tag{9c}$$

$$-i\omega\rho\phi + \rho g\kappa = 0 \qquad \text{on } \Gamma_{fs} \tag{9d}$$

$$-m_\rho\omega^2\eta - \nabla_h\left(T_\rho\,(1 - i\omega\tau)\,\nabla_h\eta\right) - i\omega\phi + g\eta = 0 \qquad \text{on } \Gamma_m \tag{9e}$$

$$\mathbf{n}\cdot\nabla\phi = 0 \qquad \text{on } \Gamma_b \tag{9f}$$

$$\mathbf{n}\cdot\nabla\phi = u_{in} \qquad \text{on } \Gamma_{in} \tag{9g}$$

$$\mathbf{n}\cdot\nabla\phi = u_{out} \qquad \text{on } \Gamma_{out} \tag{9h}$$

Eq. (9e) in frequency domain formulation enables us to draw another physical interpretation of the pre-tensioning terms. The overall transverse restoring force due to pre-tension is proportional to $T_\tau = T_\rho(1 - i\omega\tau)$. Here, the $\Re(T_\tau) = T_\rho$ corresponds to the storage modulus, which is independent of the excitation frequency. This quantity represents the potential energy stored within the membrane, as it undergoes transverse deflection. On the other hand, the imaginary part $\Im(T_\tau) = -i\omega\tau T$ represents the loss modulus, which is dependent on the excitation frequency (Sree et al., 2021). This quantity corresponds to the energy which is dissipated or extracted due to the material damping of the membrane. It should be noted that in the context of wave-energy converters, this loss modulus represents the mechanism for extracting energy. This can be through the use of dielectric materials in the membrane (Sheng et al., 2013; Mendoza et al., 2023), or other similar technologies. In the context of floating solar or floating breakwater technologies, this loss modulus represents the dissipation and partially reflection of the incoming wave energy, resulting in reduced structural loads and transverse deflections.

3. Numerical formulation

3.1. Monolithic weak form

The boundary value problem (9) is solved using a monolithic finite-element formulation, following the method proposed in Colomés et al. (2022) for VLFS. In this work, we extend this formulation to the case of floating membranes. Before describing the weak and fully discrete forms of the problem, we first introduce some notation that will be used in the sections to come.

Let us define the space of functions with absolutely integrable rth power in Ω as $L^r(\Omega)$, for $1 \le r < \infty$. In the case in which $r = 2$, we have a Hilbert space with inner product

$$(u,v)_\Omega = \int_\Omega u(\mathbf{x})\,v(\mathbf{x})\,d\Omega \tag{10}$$

and induced norm $\|u\|_{L^2(\Omega)} \equiv \|u\|_\Omega = (u,u)_\Omega^{1/2}$. Abusing of the notation, the same symbol as in (10) will be used for the integral of the product of two functions, even if these are not in $L^2(\Omega)$, and both for scalar and vector fields. The space of functions whose distributional derivatives up to order m are in $L^2(\Omega)$ are denoted by $H^m(\Omega)$. We will focus on the case of $m = 1$, which is also a Hilbert space. In addition, we will also use the inner product on a given boundary, $\Gamma \subset \Omega$, defined as

$$(u,v)_\Gamma = \int_\Gamma u(\mathbf{x})\,v(\mathbf{x})\,d\Gamma, \tag{11}$$

with the associated norm $\|u\|_{L^2(\Gamma)} \equiv \|u\|_\Gamma = (u,u)_\Gamma^{1/2}$.

Let $\mathcal{V} = H^1(\Omega)$ be a functional space in Ω, $\mathcal{V}_{\Gamma_{\text{fs}}}$ the trace space of $\mathcal{V}$ on the free surface Γ_{fs} and $\mathcal{V}_{\Gamma_{\text{m}}}$ the trace space of $\mathcal{V}$ on the structure Γ_{m}, *i.e.* $\mathcal{V}_{\Gamma_{\text{fs}}} = \{v|_{\Gamma_{\text{fs}}} : v \in \mathcal{V}\}$ and, i.e. $\mathcal{V}_{\Gamma_{\text{m}}} = \{v|_{\Gamma_{\text{m}}} : v \in \mathcal{V}\}$, respectively. We define the velocity potential $\phi \in \mathcal{V}$ and the associated test function $w \in \mathcal{V}$, the free-surface elevation function $\kappa \in \mathcal{V}_{\Gamma_{\text{fs}}}$ and its associated test function $u \in \mathcal{V}_{\Gamma_{\text{fs}}}$ and the membrane deflection $\eta \in \mathcal{V}_{\Gamma_{\text{m}}}$ with associated test function $v \in \mathcal{V}_{\Gamma_{\text{m}}}$. Note that the functional space associated to the velocity potential, $\mathcal{V}$, is defined in Ω, while the functional spaces for the free-surface elevation, $\mathcal{V}_{\Gamma_{\text{fs}}}$, and membrane elevation, $\mathcal{V}_{\Gamma_{\text{m}}}$, are defined in Γ_{fs} and Γ_{m}, respectively, leading to a mixed-dimensional problem. Using this notation, the weak form of the problem reads: *Find* $[\phi,\eta,\kappa] \in \mathcal{V}\times\mathcal{V}_{\Gamma_m}\times\mathcal{V}_{\Gamma_{fs}}$ *such that*:

$$B([\phi,\eta,\kappa],[w,v,u]) = L([w,v,u]) \qquad \forall [w,v,u] \in \mathcal{V}\times\mathcal{V}_{\Gamma_{\text{m}}}\times\mathcal{V}_{\Gamma_{\text{fs}}}. \tag{12}$$

where

$$B([\phi,\eta,\kappa],[w,v,u]) = (\nabla\phi,\nabla w)_\Omega + (\phi_t + g\kappa, \beta_h(u + \alpha_h w))_{\Gamma_{fs}} - (\kappa_t, w)_{\Gamma_{fs}} + (m_\rho\eta_{tt} + \phi_t + g\eta, v)_{\Gamma_m} \tag{13}$$

$$+ (T_\rho \nabla\eta + T_\rho \tau \nabla\eta_t, \nabla v)_{\Gamma_m} - (\eta_t, w)_{\Gamma_m} - (T_\rho \nabla\eta \cdot \mathbf{n} + T_\rho \tau \nabla\eta_t \cdot \mathbf{n}, v)_{\Lambda_m}$$

$$L([w,v,u]) = (u_{in}, w)_{\Gamma_{in}} + (u_{out}, w)_{\Gamma_{out}}. \tag{14}$$

The weak form (12) is formulated by first multiplying the governing equation Eq. (1) with test function w, integrating it over Ω and using integration by parts to obtain a reduced-order domain integral and boundary integrals. The boundary conditions in Eqs. (2) and (8a) are then substituted into the boundary integrals along Γ_b, Γ_{in}, Γ_{out}, Γ_{fs} and Γ_m. The dynamic boundary condition on Γ_{fs} Eq. (3b) is incorporated following the stabilised approach proposed in Akkerman et al. (2020). Here, the test function is modified as $\beta(\alpha w + u)$, where α is chosen based on the time-integration scheme to ensure coercivity, see Colomés et al. (2022), and β controls the contribution of the test function. The resultant Petrov–Galerkin weak form reduces the dispersion error and improves energy conservation for linear free-surface potential flow (Akkerman et al., 2020). The dynamic fluid–structure coupling boundary condition Eq. (8b) is multiplied with test-function v and the second order derivative terms are reduced using integration by parts, resulting in domain integrals along Γ_m and boundary (edge) integrals at Λ_1 and Λ_2. The final weak form is given by equation Eq. (12).

Following a similar approach, the weak form for the frequency domain boundary value problem is given by: *Find* $[\phi, \eta, \kappa] \in \mathcal{V} \times \mathcal{V}_{\Gamma_m} \times \mathcal{V}_{\Gamma_{fs}}$ *such that*:

$$B_\omega([\phi,\eta,\kappa],[w,v,u]) = L_\omega([w,v,u]) \qquad \forall [w,v,u] \in \mathcal{V} \times \mathcal{V}_{\Gamma_\mathrm{m}} \times \mathcal{V}_{\Gamma_\mathrm{fs}}, \tag{15}$$

with

$$\begin{aligned} B_\omega([\phi,\eta,\kappa],[w,v,u]) =& (\nabla\phi, \nabla w)_\Omega + (-i\omega\phi + g\kappa, \beta_h(u + \alpha_h w))_{\Gamma_{fs}} + (i\omega\kappa, w)_{\Gamma_{fs}} \\ &+ (-m_\rho \omega^2 \eta - i\omega\phi + g\eta, v)_{\Gamma_m} + (T_\rho(1 - i\omega\tau)\nabla\eta, \nabla v)_{\Gamma_m} + (i\omega\eta, w)_{\Gamma_m} \\ &- (T_\rho(1 - i\omega\tau)\nabla\eta \cdot \mathbf{n}, v)_{\Lambda_m}, \end{aligned} \tag{16}$$

$$L_\omega([w,v,u]) = (u_{in}, w)_{\Gamma_{in}} + (u_{out}, w)_{\Gamma_{out}}. \tag{17}$$

Note that the weak form for the materially undamped floating membrane is obtained by setting $\tau = 0$ in the above-mentioned equations.

3.2. Spatial discretisation

The formulation that we define in this work can be solved both, in time and frequency domain. However, in this work, we restrict ourselves to the frequency domain analysis because it is the most used approach for linear problems. The time domain analysis is straightforward, and we refer the reader to Colomés et al. (2022) for more details on the specific treatment in this case. We use a monolithic finite element solver to obtain the solution to system (15), meaning that all the unknowns are obtained by solving a fully coupled system of equations.

Let us consider a triangulation, Ω_h, of the domain Ω, leading to the conformal triangulations of the domain boundaries, $\Gamma_{\mathrm{fs},h}$, $\Gamma_{\mathrm{m},h}$, $\Gamma_{\mathrm{in},h}$, $\Gamma_{\mathrm{out},h}$ and $\Gamma_{\mathrm{b},h}$, as depicted in Fig. 1b. We define the finite-dimensional finite-element spaces for the velocity potential, free surface elevation and membrane elevation, $\mathcal{V}_h$, $\mathcal{V}_{\Gamma_{\mathrm{fs}},h}$ and $\mathcal{V}_{\Gamma_{\mathrm{m}},h}$, respectively, as follows:

$$\mathcal{V}_h = \left\{ w_h \in C^0(\Omega) : \ w_h|_K \in \mathbb{P}_r(K), \forall K \in \Omega_h \right\}, \tag{18}$$

$$\mathcal{V}_{\Gamma_{\mathrm{fs}},h} = \left\{ w_h|_E : \ w_h \in \hat{\mathcal{V}}_h, \forall E \in \Gamma_{\mathrm{fs},h} \right\}, \tag{19}$$

$$\mathcal{V}_{\Gamma_{\mathrm{m}},h} = \left\{ w_h|_E : \ w_h \in \hat{\mathcal{V}}_h, \forall E \in \Gamma_{\mathrm{m},h} \right\}, \tag{20}$$

where $\mathbb{P}_r(K)$ is the space of Lagrange polynomials of degree r in an element K, and E are facets of dimension $d-1$, with d being the topological dimension of the domain Ω. Using this notation, the final discrete form in the frequency domain reads: *Find* $[\phi_h, \eta_h, \kappa_h] \in \mathcal{V}_h \times \mathcal{V}_{\Gamma_m,h} \times \mathcal{V}_{\Gamma_{fs},h}$ *such that*

$$B_\omega([\phi_h,\eta_h,\kappa_h],[w_h,v_h,u_h]) = L_\omega([w_h,v_h,u_h]) \qquad \forall [w_h,v_h,u_h] \in \mathcal{V}_h \times \mathcal{V}_{\Gamma_{\mathrm{m}},h} \times \mathcal{V}_{\Gamma_{\mathrm{fs}},h}, \tag{21}$$

with B_ω and L_ω as defined in (16) and (17), respectively.

3.3. Consistency and energy conservation of the discrete form

It can be demonstrated that the discrete form defined in (21) is well posed, that is, it has a unique solution. This can be proven by following an analogous process as the one defined in chapter 4 of Colomés et al. (2022). In order to limit the scope of this paper, we will only prove the statements of consistency of the solution and energy conservation.

Proposition 1 (*Consistency*). *The discrete problem* (21) *is consistent. That is, the exact solution* $[\phi, \kappa, \eta] \in \mathcal{V} \times \mathcal{V}_{\Gamma_{fs}} \times \mathcal{V}_{\Gamma_m}$ *satisfies the approximate problem*

$$B_\omega([\phi,\kappa,\eta],[w_h,v_h,u_h]) = L_\omega([w_h,v_h,u_h]) \quad \forall [w_h,v_h,u_h] \in \mathcal{V}_h \times \mathcal{V}_{\Gamma_{fs},h} \times \mathcal{V}_{\Gamma_m,h}. \tag{22}$$

Proof. The consistency statement results from integrating by parts on each element the terms $(\nabla\phi, \nabla w_h)_{\Omega_h}$ and $(T_\rho(1 - i\omega\tau)\nabla\eta, \nabla v_h)_{\Gamma_{m,h}}$ appearing in (16), using the strong form of the Eqs. (9a) and boundary conditions (9d)–(9h). □

Proposition 2 (*Energy Conservation*). *The discrete problem (21) is energy conserving for any β_h such that $0 < \beta_h < 1$. That is,*

$$\frac{dE_{total}}{dt} = -P_{dis,str}. \tag{23}$$

With

$$E_{total} = E_{kin,flow} + E_{pot,flow} + E_{kin,str} + E_{ela,str}, \tag{24}$$

and

$$E_{kin,flow} = \frac{1}{2}\|\nabla\phi\|^2_\Omega, \tag{25a}$$

$$E_{pot,flow} = \frac{g}{2}\left(\|\kappa\|^2_{\Gamma_{fs}} + \|\eta\|^2_{\Gamma_m}\right), \tag{25b}$$

$$E_{kin,str} = \frac{1}{2}\left\|m_\rho\,\eta_t\right\|^2_{\Gamma_m}, \tag{25c}$$

$$E_{ela,str} = \frac{1}{2}\left\|T_\rho\,\nabla\eta\right\|^2_{\Gamma_m}, \tag{25d}$$

$$P_{dis,str} = \left\|T_\rho\tau\,\nabla\eta_t\right\|^2_{\Gamma_m}. \tag{25e}$$

Proof. Let us select the set of test functions as $[w_h, v_h, u_h] = \left[-i\omega\phi_h, \frac{-i\omega}{\beta}\kappa_h + i\omega\alpha_f\phi_h, -i\omega\eta_h\right] \in \mathcal{V}_h \times \mathcal{V}_{\Gamma_{fs},h} \times \mathcal{V}_{\Gamma_m,h}$. Introducing them into (21) we have that, for $u_{in} = u_{out} = 0$ and $\nabla\eta \cdot \mathbf{n} = 0$, the following statement holds

$$\begin{aligned} 0 =& B_\omega([\phi_h, \kappa_h, \eta_h], [-i\omega\phi_h, \frac{-i\omega}{\beta}\kappa_h + i\omega\alpha_f\phi_h, -i\omega\eta_h]) - L_\omega([-i\omega\phi_h, \frac{-i\omega}{\beta}\kappa_h + i\omega\alpha_f\phi_h, -i\omega\eta_h]) \\ =& (\nabla\phi_h, -i\omega\nabla\phi_h)_\Omega + (g\kappa_h, -i\omega\kappa_h)_{\Gamma_{fs}} + (-m_\rho\omega^2\eta_h, -i\omega\eta_h)_{\Gamma_m} + (g\eta_h, -i\omega\eta_h)_{\Gamma_m} + (T_\rho\nabla\eta_h, -i\omega\nabla\eta_h)_{\Gamma_m} \\ &+ (-i\omega\tau T_\rho\nabla\eta_h, -i\omega\nabla\eta_h)_{\Gamma_m}. \end{aligned} \tag{26}$$

Introducing back the time-domain transformation defined in Section 2.4 into Eq. (26) and using the energy definitions (24)–(25), leads to the following statement

$$\begin{aligned} 0 =& \frac{d}{dt}\left(\frac{1}{2}\|\nabla\phi_h\|^2_\Omega\right) + \frac{d}{dt}\left(\frac{1}{2}g\|\kappa_h\|^2_{\Gamma_{fs}}\right) + \frac{d}{dt}\left(\frac{1}{2}m_\rho\|\eta_{h,t}\|^2_{\Gamma_m}\right) + \frac{d}{dt}\left(\frac{1}{2}g\|\eta_h\|^2_{\Gamma_m}\right) + \frac{d}{dt}\left(\frac{1}{2}T_\rho\|\nabla\eta_h\|^2_{\Gamma_m}\right) \\ &+ \left(\tau T_\rho\|\nabla\eta_{h,t}\|^2_{\Gamma_m}\right) = \frac{dE_{\text{total}}}{dt} + P_{\text{dis,str}}. \end{aligned} \tag{27}$$

which proves Proposition 2. Note that the selection for v_h imposes a mild compatibility requirement on the discretisation spaces in order for the proof to hold, viz. $\gamma_{\Gamma_{fs}}(\mathcal{V}) \in \mathcal{V}_{\Gamma_{fs}}$. □

3.4. Wave generation and wave damping zones

The waves in the numerical domain are generated using the Neumann boundary condition Eq. (2b) on Γ_{in}, where u_{in} is prescribed using the linear Airy's wave theory. An additional damping zone of length L_d is placed adjacent to Γ_{in}, as shown in Fig. 1. This damping zone Ω_d will absorb the waves reflected by the floating membrane. Inside the damping zone, we apply an artificial wave damping function on the free-surface boundary Γ_d, based on the $\phi_n - \eta$ type *Method 5* outlined in Kim et al. (2014). This is summarised in Eq. (28), where μ_1 and μ_2 are the damping functions, k is the wavenumber, x_0 denotes the starting-point of the damping zone. Eq. (28) includes terms for prescribing the input wave elevation η_{in} and input velocity potential ϕ_{in} at the free-surface along the length of the damping zone, facilitating selective absorption of waves reflected by the membrane. We prescribe the input quantities η_{in} and ϕ_{in} using the linear Airy's wave theory. Further details regarding the methodology, conservation properties, and accuracy of this damping zone method can be found in Kim et al. (2014). As per the conclusions in Kim et al. (2014), the $\phi_n - \eta$ method has been shown to effectively absorb nonlinear, multi-directional and irregular waves.

The outgoing waves are absorbed on Γ_{out} using the Neumann boundary condition Eq. (2c). Here, the u_{out} for linear waves is prescribed following the Sommerfeld radiation boundary condition, given by Eq. (29) in the frequency domain formulation. In certain cases, an additional damping zone Ω_d is placed next to Γ_{out} to improve the absorbance of outgoing waves.

$$\begin{aligned} &\text{DFSC on } \Gamma_d \qquad \frac{\partial\phi}{\partial t} = -g\kappa - \mu_1\left(\frac{\partial\phi}{\partial n} - \frac{\partial\phi_{in}}{\partial n}\right) \\ &\text{KFSC on } \Gamma_d \qquad \frac{\partial\eta}{\partial t} = \frac{\partial\phi}{\partial z} - \mu_2(\kappa - \kappa_{in}) \\ &\text{where} \qquad \mu_1 = \mu_0\left(1 - \sin\left(\frac{\pi}{2}\frac{x - x_0}{L_d}\right)\right), \quad \text{and} \quad \mu_2 = k\mu_1 \end{aligned} \tag{28}$$

$$\nabla\phi \cdot \mathbf{n} = ik\phi \qquad \text{on } \Gamma_{out} \tag{29}$$

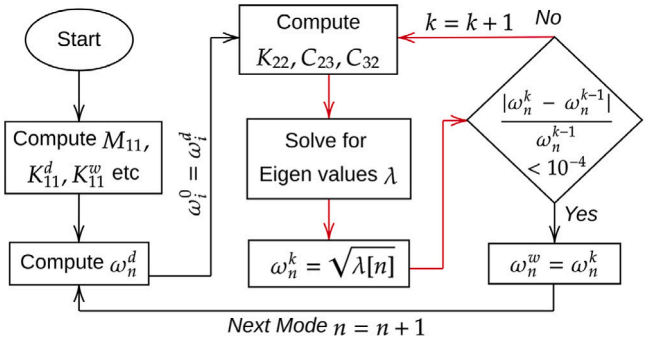

Fig. 2. Iterative algorithm for determining the wet natural frequencies and mode shapes of the floating membrane.

4. Natural frequencies and mode shapes of materially undamped floating membrane

Modal analysis for a membrane in the absence of surrounding fluid will depend on the material properties and the structural design; and is termed as the dry modal analysis. However, the free-vibration of a floating membrane will be influenced by the acceleration of the surrounding fluid (added-mass) and the additional hydrostatic-gravitational stiffness. The modal analysis accounting for these effects is termed as wet modal analysis.

The present work uses the linearised frequency domain weak form Eq. (15), with $\tau = 0$, for deriving the expressions for added mass and added stiffness for the materially undamped floating membrane. As mentioned in Section 3.1, the function u, v and w are the basis functions for unknowns κ, η and ϕ, respectively. Therefore, the estimates of these unknowns within an element are given by $\eta_h = \sum_i v_{h,i}\,\eta_{P,i}$, $\phi_h = \sum_j w_{h,j}\,\phi_{P,j}$, and $\kappa_h = \sum_k u_{h,k}\,\kappa_{P,k}$, where $\eta_{P,i}$, $\phi_{P,j}$ and $\kappa_{P,k}$ are the degrees of freedom. Using this notation, the weak form Eq. (15) is split into the membrane, free-surface and fluid equations with diagonal and coupling terms as shown in Eq. (30).

$$\begin{bmatrix} -\omega^2\mathbf{M}_{11} + \mathbf{K}^d_{11} + \mathbf{K}^w_{11} & -i\omega\mathbf{C}_{12} & 0 \\ i\omega\mathbf{C}_{21} & \mathbf{K}_{22} & \mathbf{C}_{23} \\ 0 & \mathbf{C}_{32} & \mathbf{K}_{33} \end{bmatrix} \begin{bmatrix} \boldsymbol{\eta}_P \\ \boldsymbol{\phi}_P \\ \boldsymbol{\kappa}_P \end{bmatrix} = \begin{bmatrix} \mathbf{F}_\eta \\ \mathbf{F}_\phi \\ \mathbf{F}_\kappa \end{bmatrix} \tag{30}$$

Where $\boldsymbol{\eta}_P = \{\eta_{P,i}\}$, $\boldsymbol{\phi}_P = \{\phi_{P,i}\}$ and $\boldsymbol{\kappa}_P = \{\kappa_{P,i}\}$. This mixed-domain system will have square diagonal matrices $(\mathbf{M}, \mathbf{K})$ and rectangular non-diagonal coupling matrices $(\mathbf{C})$. These matrices are defined as follows. Here we use the free-edge boundary condition at the membrane edges Λ_m.

$$\begin{aligned} &\mathbf{M}_{11} = (m_\rho v_h,\, v_h)_{\Gamma_m} && \mathbf{K}^d_{11} = (T_\rho \nabla v_h,\, \nabla v_h)_{\Gamma_m} \\ &\mathbf{K}^w_{11} = (g v_h,\, v_h)_{\Gamma_m} && \mathbf{K}_{22} = (\nabla w_h,\, \nabla w_h)_\Omega - (ik w_h,\, w_h)_{\Gamma_{in},\Gamma_{out}} \qquad \mathbf{K}_{33} = (g u_h,\, u_h)_{\Gamma_{fs}} \\ &\mathbf{C}_{12} = (w_h,\, v_h)_{\Gamma_m} && \mathbf{C}_{21} = (v_h,\, w_h)_{\Gamma_m} \\ &\mathbf{C}_{23} = (i\omega u_h,\, w_h)_{\Gamma_{fs}} && \mathbf{C}_{32} = (-i\omega w_h,\, u_h)_{\Gamma_{fs}} \end{aligned} \tag{31}$$

The matrix $\mathbf{K}^d_{11}$ is presented for free-edge boundary condition. For the free-vibration analysis, the external forcing terms $F_\eta = 0$, $F_\phi = 0$, $F_\kappa = 0$. Further, the boundary integrals on Γ_{in} and Γ_{out} are used to apply the radiation boundary condition $\nabla\phi \cdot \mathbf{n} = ik\phi$, as seen in K_{22}. It should be noted that the matrices $\mathbf{K}_{22}$, $\mathbf{C}_{23}$ and $\mathbf{C}_{32}$ are dependent on frequency ω.

The dry modes of the membrane are determined through eigenvalue analysis of Eq. (32).

$$(-\omega^2\mathbf{M}_{11} + \mathbf{K}^d_{11})\,\eta^P = 0 \tag{32}$$

In order to determine the wet modes of the floating membrane, the matrix equation Eq. (30) is written in terms of η^P through the process of elimination of variables. This results in an undamped spring-mass system with added mass $\mathbf{A}$ and added stiffness $\mathbf{K}^w_{11}$, as shown in Eq. (33).

$$\begin{aligned} &(-\omega^2(\mathbf{M}_{11} + \mathbf{A}) + \mathbf{K}^d_{11} + \mathbf{K}^w_{11})\,\eta^P = 0 \\ &\text{where} \quad \mathbf{A} = \mathbf{C}_{12}\mathbf{M}_\phi^{-1}\mathbf{C}_{21}, \quad \mathbf{M}_\phi = \mathbf{K}_{22} - \mathbf{C}_{23}\mathbf{K}_{33}^{-1}\mathbf{C}_{32} \end{aligned} \tag{33}$$

The added mass $\mathbf{A}$ depends on frequency ω because of the coefficients $\mathbf{K}_{22}$, $\mathbf{C}_{23}$ and $\mathbf{C}_{32}$. Therefore, this wet eigenvalue problem is nonlinear. For each mode, we follow the iterative algorithm shown in Fig. 2 to solve for the natural frequency and the corresponding mode shape. In Section 5.2, we present calculated the Eigen frequencies and mode shapes for a membrane, and analyse their dependence on the material and design properties.

5. Numerical results

The finite-element formulation and modal analysis were numerically implemented in *Julia* programming language (Bezanson et al., 2017), using the *Gridap* finite element library (Badia and Verdugo, 2020). This library enables high-level implementation of

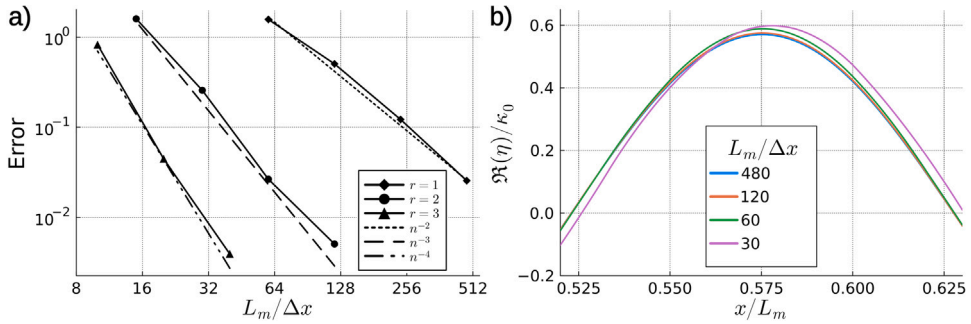

Fig. 3. (a) Plots showing the computed numerical error with the increasing number of elements, using elements of polynomial degree $r = 1, 2, 3$. (b) Plots showing the evolution of the numerical solution for η, obtained using quadratic polynomial shape function for various numbers of elements.

the formulation, resembling the mathematical notations in weak form. The *Gridap* library efficiently assembles internal loops based on this notation-based expression, optimised for the high-performance *Julia* JIT compiler. A comprehensive software implementation of *Gridap* is available in Verdugo and Badia (2022). These features enable swift prototyping of the finite-element program, and exhibit excellent computational performance. Critically, *Grdiap*, possesses the ability to assemble finite-element formulation over mixed-dimensions and mixed-order. This feature is of utmost importance because the monolithic floating viscoelastic membrane problem necessitates a formulation over a fluid domain and the attached membrane surface. The program used to generate the results for this manuscript is similar to the registered *Julia* package (Colomes Gene, 2022).

5.1. Convergence analysis

The spatial convergence analysis for the numerical model is conducted by studying the elastic response of a finite floating membrane to a monochromatic incoming wave in frequency domain formulation. The analysis is conducted in a 2D vertical numerical domain with a constant water-depth of $h = 10$ m and a domain length of $L_\Omega = 21h$. The incoming waves are generated using the left boundary Γ_{in}. A damping zone Ω_d of length $L_d = 6h$ is placed adjacent to Γ_{din} to absorb the waves reflected by the floating membrane. The outgoing waves are absorbed using the radiation boundary condition Eq. (29) applied on Γ_{out}. A floating membrane of length $L_m = 3h$, mass per unit area $m = 0.9\rho$, and tension $T = 0.9\rho g$ is located at a distance of $12h$ from Γ_{in}. The present analysis is carried out using free-edge boundary condition Eq. (7b) for the membrane. A membrane with these properties is expected to generate significant deflection which is ideal for visualising the convergence of the solution. The floating membrane is exposed to linear regular waves corresponding with $\omega = 2.0\ \mathrm{rad\,s^{-1}}$ and amplitude $\kappa_0 = 0.025h$.

The domain is meshed as a Cartesian grid with rectangular elements having uniform Δx and Δz. The analysis is conducted for linear, quadratic and cubic polynomial shape functions. The convergence rate is monitored using the L^2 norm, given by the following Eq. (34).

$$\text{Error} = \| \eta - \eta_{ref} \|_{L^2(\Gamma_m)} \overset{\text{def}}{=} \sqrt{\int_{\Gamma_m} | \eta - \eta_{ref} |^2 \, d\Gamma_m} \tag{34}$$

Here, η_{ref} is the solution obtained using the smallest mesh size and cubic polynomial shape function. We report the error in the numerical solution for various mesh sizes and polynomial orders. Fig. 3a reports the computed convergence rate for elements of polynomial degree r and its comparison against the optimal convergence rate $O(r+1)$. Fig. 3b reports the evolution of the numerical solution at the crest, obtained using quadratic polynomial ($r = 2$) shape function, for various mesh sizes. From these results, it is concluded that the presented model has an optimal rate of convergence.

5.2. Natural frequencies of 1D finite floating membrane

This section employs the iterative algorithm described in Section 4 for studying wet mode shapes and corresponding natural frequencies for a finite, materially undamped, floating membrane. The analysis is done for a membrane of length L_m with free-edge boundary condition, placed in a domain with water-depth h and domain length $L_\Omega = 3L_m$. This analysis does not require the generation of incoming waves. Therefore, the domain does not contain any damping zones and the boundaries Γ_{in} and Γ_{out} are both set to radiation boundary condition, Eq. (29). After conducting a convergence analysis similar to the one in Section 5.1, we employ rectangular elements with quadratic polynomial shape function. Further, these elements have a uniform $\Delta x = 0.025L_m$, while the Δz increases exponentially from $\Delta z = 0.038h$ at the free-surface to $\Delta z = 0.2h$ at the bottom boundary across a span of 10 intervals. This mesh configuration is computationally efficient as it ensures a greater number of elements are allocated to capture the larger gradients along the free surface.

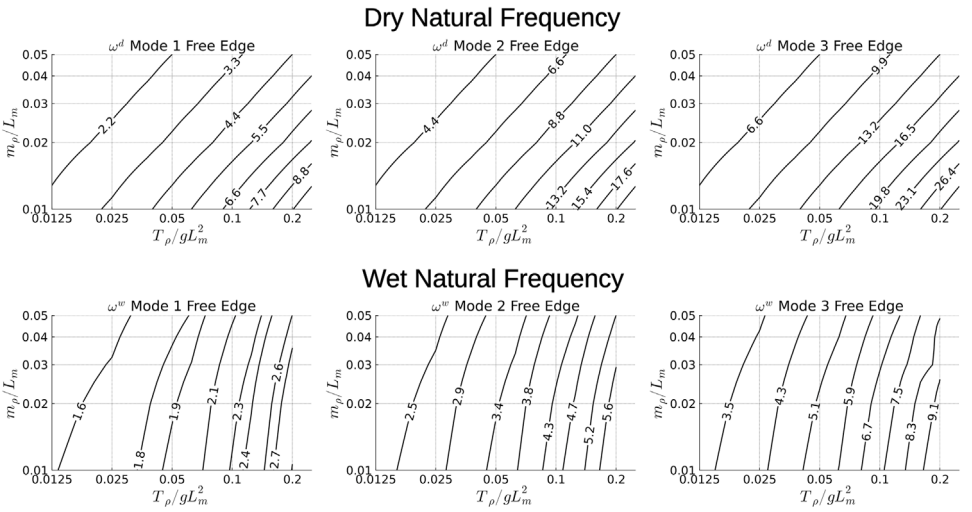

Fig. 4. Contour plots of variations in dry natural frequency ω^d, wet natural frequency ω^w for the first three elastic modes, over a range of mass and tension of the membranes with free-edge boundary condition. The values of T_ρ/gh^2 and m_ρ/L_m are plotted on $\log_{10}$ axis.

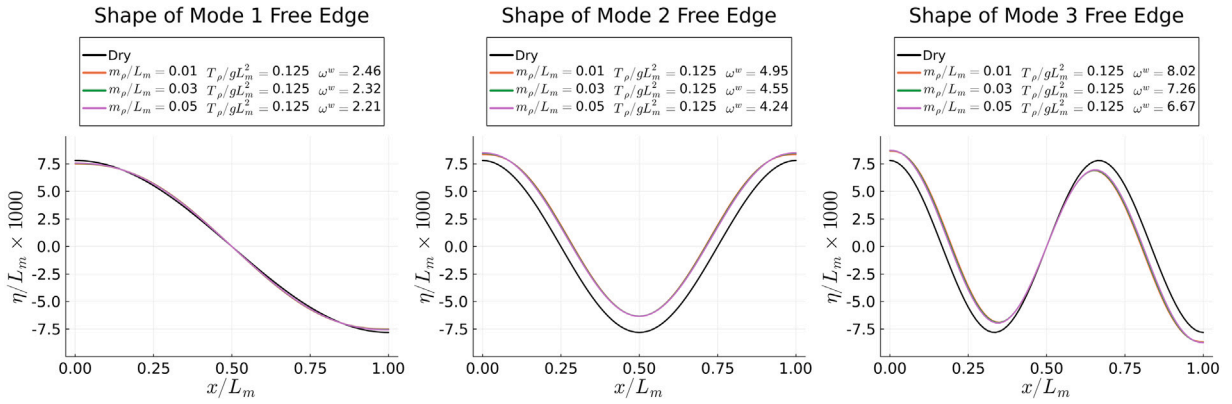

Fig. 5. Plots of first three elastic wet mode shapes for floating membranes with same T_ρ and different m_ρ, compared against corresponding dry mode shapes.

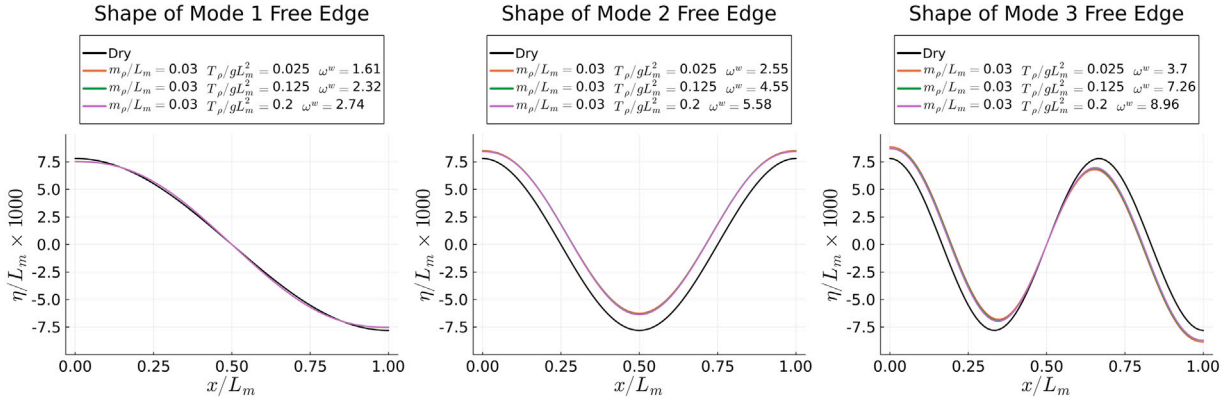

Fig. 6. Plots of first three elastic wet mode shapes for floating membranes with same m_ρ and different T_ρ, compared against corresponding dry mode shapes.

The numerical tests were conducted on a range of thin-floating membranes with free-edge boundary condition, characterised by draft $m_\rho/L_m \in [0.01, 0.05]$ and $T_\rho/gL_m^2 \in [0.0125, 0.2]$, in deep-water conditions. The analytical expression for dry natural frequency ω_n^d for mode n is given by Eq. (35).

$$\omega_n^d = n\pi\sqrt{\frac{T_\rho/L_m^2}{m_\rho}} \implies \log(\omega_n^d) = \log(n\pi) + \frac{1}{2}\log\left(\frac{T_\rho}{L_m^2}\right) - \frac{1}{2}\log(m_\rho) \tag{35}$$

Fig. 4 presents the numerically obtained values of ω_n^d, calculated through eigenvalue analysis based on Eq. (32). We evaluate the accuracy of the numerically obtained values of ω_n^d against the analytical expression for ω_n^d given in Eq. (35). The root mean square difference between numerical and analytical values of ω_n^d, for the plotted range of m_ρ/L_m and T_ρ/gL_m^2, is 1.42×10^{-7} for Mode 1, 4.55×10^{-6} for Mode 2 and 3.45×10^{-5} for Mode 3.

The wet natural frequency is obtained using the eigen-value analysis of Eq. (33), following the iterative algorithm in Fig. 2. We illustrates the variation of wet natural frequency ω_n^w for a range of m_ρ/L_m and T_ρ/gL_m^2 in Fig. 4. For the floating membrane, the natural frequency is influenced by the hydrostatic stiffness of the water-plane area and the added mass due to the presence of surrounding fluid. It is noteworthy that ω_n^w is consistently lower than ω_n^d within the tested range, indicating a dominating influence of added mass. Compared to ω_n^d, ω_n^w demonstrates reduced sensitivity to the mass m_ρ of the membrane, particularly for high frequency modes. Based on this analysis, it is concluded that the wet natural frequency of the floating membrane can be primarily adjusted by controlling its tension T_ρ.

We further analyse the mode shapes for both the dry and wet modes of the membrane. Fig. 5 shows the comparison of wet and dry mode shapes for membranes, while keeping the tension constant and varying the mass. Fig. 6 presents the same, while keeping the mass constant and varying the tension in the membrane. The dry mode shape for a particular mode remains consistent regardless of the membrane's mass and tension. For each mode, a single plot adequately represents the dry mode shape, characterised by regular sinusoidal patterns. In contrast, while the wet mode shapes closely resembles a sinusoidal pattern, they are not perfectly sinusoidal. As a result, distinctions between the wet and dry mode shapes are discernible in Fig. 5 and Fig. 6.

5.3. Frequency domain solution of 1D finite floating membrane

Having completed the convergence and modal analysis, we proceed to examine the response of 1D finite floating membrane in a 2D fluid domain, subjected to linear regular waves. The water depth is set at a constant value of h, and the length of the finite floating membrane is L_m. The total length of the domain is $16.5L_m$. The incoming progressive waves are generated using the Neumann boundary condition Eq. (9g) on Γ_{in}, with the analytical expression for ϕ_{in} and η_{in} based on linear wave theory. Furthermore, a damping zone Ω_d of length $L_d = 7.5L_m$ is placed adjacent to Γ_{in}, in the range $x \in [-7.5L_m, 0]$, in order to absorb the waves reflected by the floating membrane, (refer to the schematic in Fig. 1). The outgoing waves are captured using the radiation boundary condition Eq. (29) on Γ_{out}. No additional damping zone is placed adjacent to Γ_{out}. The floating membrane is placed between $x \in [4L_m, 5L_m]$ to provide a space of $4L_m$ on both sides of the membrane. This configuration facilitates the observation and analysis of the reflected and transmitted waves upstream and downstream from the membrane.

The computational domain is discretised using second-order quadrilateral elements, with a constant $\Delta x = 0.01L_m$, while the Δz varies exponentially over 20 elements from $\Delta z = 0.0054h$ near the free-surface to $\Delta z = 0.17h$ near the bottom boundary. This configuration is chosen following the convergence analysis from Section 5.1, considering the structural response, and the wave-length and steepness of the shortest wave. This results in 33000 second-order quadrilateral elements. The simulations are executed on a system with Intel(R) Core(TM) i5-11320H processor and 32 GB RAM. For this numerical setup, the run-time for the simulations is 4.5 s per frequency.

A number of probes are placed throughout the domain for gathering data. Let κ_{in}, κ_r and κ_t be the complex-valued space varying solutions for incoming waves, reflected waves upstream of the membrane and transmitted waves downstream of the membrane, respectively. The incoming regular wave is generated with an amplitude of $\kappa_0 = |\kappa_{in}|$. Upstream of the membrane, three probes are placed at $x_{p1} = 2.635L_m$, $x_{p2} = 2.685L_m$ and $x_{p3} = 2.75L_m$ to extract the reflected wave κ_r solution using the least-squares method (Mansard and Funke, 1980). The downstream transmitted wave κ_t is measured using a single probe at $x_{p4} = 6.25L_m$. These observations are used for reporting the reflection and the transmission coefficients $K_R = \frac{P_R}{P_{in}}$ and $K_T = \frac{P_T}{P_{in}}$. The energy absorbed by the materially-damped floating membrane $\tau \neq 0$ is reported using absorption coefficient $K_A = \frac{P_A}{P_{in}}$. If the proportional damping mechanism represents the power extracted by a wave-energy converter, then K_A can be termed as its capture width. The expressions for input P_{in}, reflected P_R and transmitted P_T wave power per unit width, averaged over a wave-period are given by the following Eqs. ((36)a-c) (Dean and Dalrymple, 1991, Chapter 4).

$$P_{in} = \frac{1}{2}\rho g|\kappa_{in}|^2 C_g \qquad \text{where } C_g = \frac{\omega}{k}\frac{1}{2}\left(1 + \frac{2kh}{\sinh(2kh)}\right) \tag{36a}$$

$$P_R = \frac{1}{2}\rho g|\kappa_r|^2 C_g \tag{36b}$$

$$P_T = \frac{1}{2}\rho g|\kappa_t|^2 C_g \tag{36c}$$

$$P_A = \frac{1}{t_{wave}}\int_t^{t+t_{wave}}\left(\int_{\Gamma_m} P_{\text{dis,str}}\, d\Gamma_m\right) dt = \frac{1}{2}\rho T_\rho \tau\omega^2 \int_{\Gamma_m} |\nabla\eta|^2\, d\Gamma \tag{36d}$$

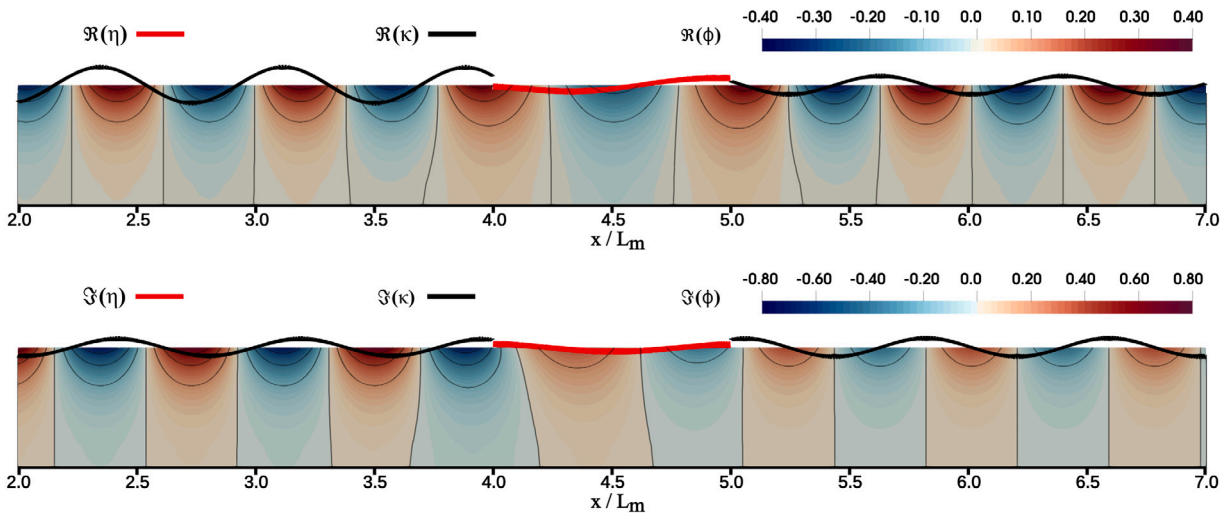

Fig. 7. Contour plot of solution of ϕ in the vicinity of the floating membrane, for $\omega = 2.0$ rad s^{-1} and $\tau = 0.0$, highlighting the elongation of the wave underneath the membrane. Exaggerated plots of the surface-elevation κ and membrane deflection η.

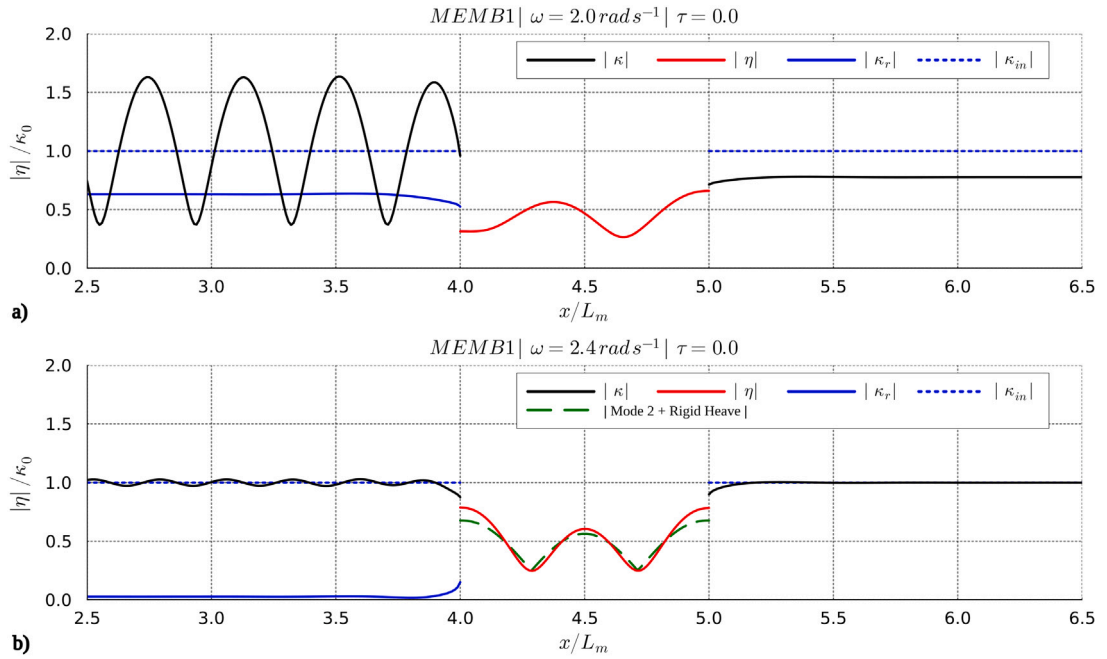

Fig. 8. Plots of magnitude of the complex solution along the domain length for total free-surface elevation κ, membrane deflection η, reflected wave κ_r and incoming wave κ_{in}. (a) $\omega = 2.0$ rad s^{-1} and $\tau = 0.0$, (b) $\omega = 2.4$ rad s^{-1} and $\tau = 0.0$.

Here Eq. (36d) is the expression for P_A, power absorbed or dissipated by the viscoelastic membrane per unit width, averaged over a wave period t_{wave}. This is derived using the dissipated power expression $P_{\text{dis,str}}$ from Eq. (25e).

The wave reflection and transmission coefficients are often expressed as $C_R = \frac{\kappa_r}{\kappa_{in}}$ and $C_T = \frac{\kappa_t}{\kappa_{in}}$. However, in our study, we opt to represent wave reflection and transmission coefficients as $K_R = \frac{P_R}{P_{in}}$ and $K_T = \frac{P_T}{P_{in}}$ for two reasons: (1) The absorption coefficient $K_A = \frac{P_a}{P_{in}}$ lacks an equivalent expression $C_A = \frac{\kappa_a}{\kappa_{in}}$ due to the absence of a physical "absorbed wave amplitude" κ_a. Therefore, our chosen coefficients enable us to present reflection, transmission, and absorption in a consistent manner; and (2) Our choice of these coefficient offers readers a direct representation of the proportional wave energy reflected, transmitted, and absorbed by the viscoelastic membrane.

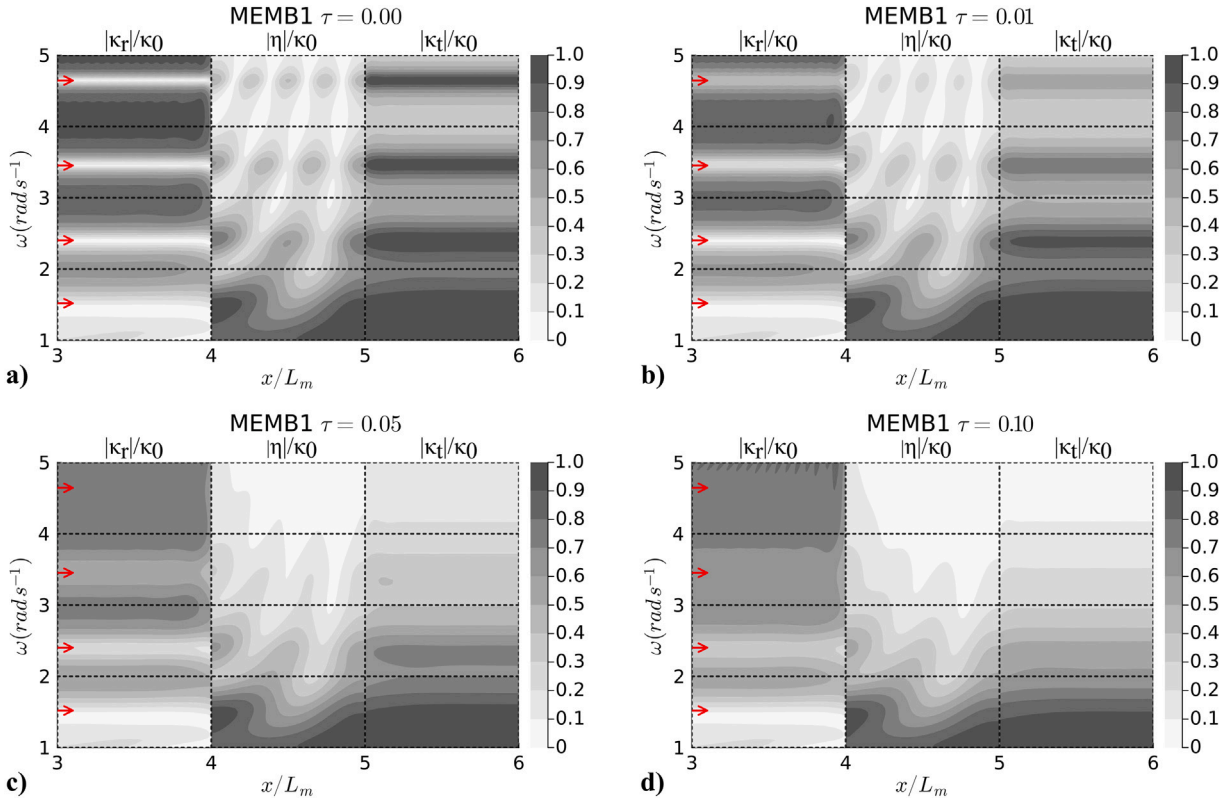

Fig. 9. Contour plots of amplitude of the deflection η, reflected wave κ_r and transmitted wave κ_t in the vicinity of the membrane *MEMB1* for $\omega \in [0.7, 5.0]$. (a) $\tau = 0.0$, (b) $\tau = 0.01$, (c) $\tau = 0.05$, (d) $\tau = 0.10$. The arrows indicate the wet natural frequency of *MEMB1* having $\tau = 0$.

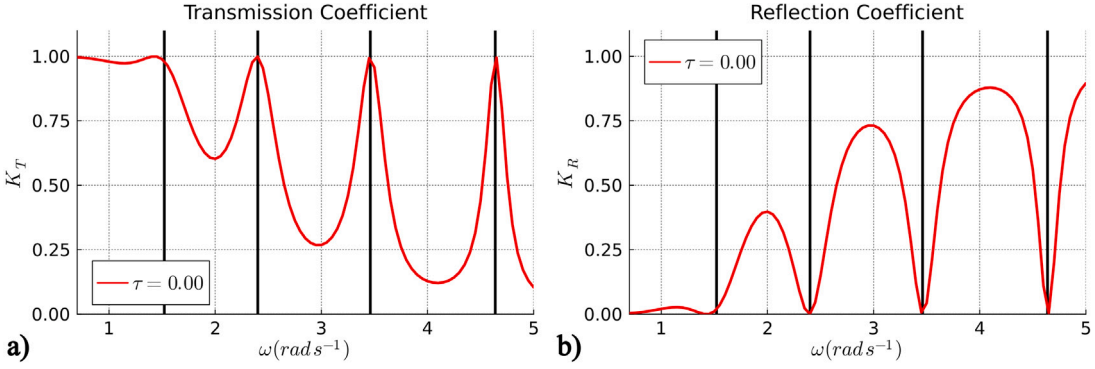

Fig. 10. Plots of reflection and transmission coefficient for regular waves interaction with floating membrane *MEMB1* with $\tau = 0$. The vertical lines are natural frequencies of the wet modes of *MEMB1*.

5.3.1. No material damping

We consider a membrane *MEMB1* of length $L_m = 2h$, $T_\rho/gL_m^2 = 0.025$, $m_\rho/L_m = 0.045$, floating in still-water depth $h = 10$ m with free-edge boundary condition. These parameter settings align with those employed in the BEM analysis of Trivedi and Koley (2022). The problem will be solved using the frequency-domain approach, as described in Section 3.1. Following the analysis from Section 5.2, the first four wet natural frequencies of *MEMB1* are $\omega^w_{1-4} = \{1.55322.41363.46694.6418\}$ rad s^{-1}. These values can be contrasted against the dry natural frequencies of *MEMB1* $\omega^d_{1-4} = \{1.6400, 3.2805, 4.9217, 6.5642\}$ rad s^{-1}. We once again highlight the significant difference between ω^w and ω^d values resulting from the added-mass and stiffness due to the presence of the fluid.

The next step is to examine the interaction of regular waves with *MEMB1* having no material damping, i.e., $\tau = 0$. The first test is conducted using monochromatic waves κ_{in} with $\omega = 2.0$ rad s^{-1}, in between its ω^w_1 and ω^w_2, with the wave-amplitude $\kappa_0 = |\kappa_{in}| = 0.1$ m. The resultant solution for ϕ throughout the domain Ω, η on Γ_m and κ on Γ_{fs} are presented in Fig. 7. The figure

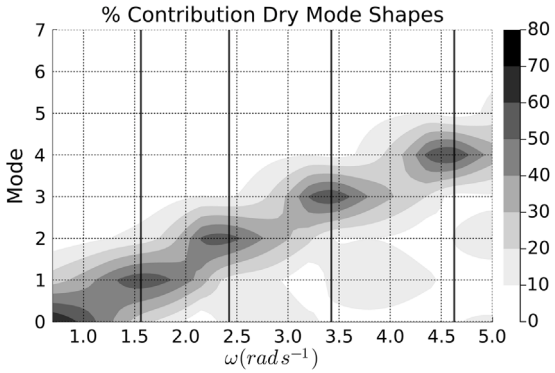

Fig. 11. Contour plots illustrating the proportional contribution of the dry mode shapes of *MEMB1* in the elastic response of the floating membrane *MEMB1* across a range of frequencies for $\tau = 0$.

highlights the deflection of the floating membrane, accompanied by partial reflection and transmission of the incoming waves, and stretching of the waves underneath the membrane. The magnitude of the solution for surface elevation κ in the vicinity of the membrane and the deflection η of the membrane are presented in Fig. 8a. This figure further decomposes the upstream solution for κ into incoming wave κ_{in} and reflected wave $\kappa_r = \kappa - \kappa_{in}$. Given the 2D nature of this problem setting, the downstream solution for κ is equal to the transmitted wave κ_t. It is observed that the magnitude of reflected and transmitted waves is steady away from the membrane. We can also observe the presence of evanescent waves in both the κ_r and κ_t plots in the vicinity of the membrane. The figure further highlights a higher magnitude for the transmitted waves compared to the reflected waves, quantified as reflection coefficient $K_R = 0.3976$ and transmission coefficient $K_T = 0.6025$.

The observed discontinuity between free-surface elevation and membrane deflection is expected in this linearised problem. Continuity between κ and η is not enforced in this analysis, as it would lead to an over-constrained system. Furthermore, the formulation does not necessitate continuity between κ and η since these are treated as two distinct boundaries of the domain, interconnected solely by the velocity potential ϕ. Fig. 7 underscores the required continuity in the velocity potential ϕ at the interfaces between the fluid underneath the membrane and outside the membrane.

We repeat the same analysis using incoming monochromatic waves with $\omega = 2.4\ \mathrm{rad\,s^{-1}}$, which is very close to the second elastic wet mode of the membrane with $\omega_2^w = 2.4136\ \mathrm{rad\,s^{-1}}$. In this case, the incoming wave is nearly completely transmitted by the floating membrane, as seen in Fig. 8b. The values of reflection and transmission coefficient are $K_R = 0.0007$ and $K_T = 0.9992$ respectively. In Section 5.2 we calculated the elastic mode shapes for the membrane. In Fig. 8b, we superimpose the magnitude of the second elastic mode plus the rigid heave motion. This overlay allows us to contrast the obtained deflection with the second elastic mode shape, highlighting the strong presence of this elastic mode.

This analysis is repeated for regular waves in frequency range $\omega \in [0.7, 5]\ \mathrm{rad\,s^{-1}}$. Fig. 9a presents the magnitude of the solution for membrane deflection η, reflected wave κ_r and transmitted wave κ_t in the vicinity of the membrane for the tested frequency range. From the figure we can observe that the lower wave frequencies produce a larger deflection in the membrane, while the higher frequencies result in relatively small membrane deflection. Additionally, it is evident that the membrane largely transmits the lower frequencies and reflects the higher frequencies. This observation is quantified as the reflection and transmission coefficient K_R and K_T as shown in Fig. 10. The arrows in Fig. 9 and the vertical lines in Fig. 10 correspond to the wet natural frequencies of *MEMB1* with $\tau = 0$. From these figures, it is distinctly evident that waves aligning with the wet natural frequencies of the membrane are fully transmitted. Therefore, the materially undamped membrane ($\tau = 0$) behaves like a mechanical filtering, largely transmitting waves with frequencies corresponding to its wet natural frequencies.

In Section 4, we obtained the shapes of the wet and the dry elastic modes of the membrane. The steady-state response of the floating membrane can be expanded as a series of dry modes. Fig. 11 presents the contour plots of the relative contribution of each dry elastic mode in the elastic response of *MEMB1* across a range of wave frequencies.

5.3.2. *Including material damping*

The simulation setup from Section 5.3.1 was used to test the response of the floating membrane to regular waves, now including the material damping ($\tau \neq 0$). Fig. 12 shows the solution for ϕ, η and κ for the case of $\omega = 2.0\ \mathrm{rad\,s^{-1}}$ and $\tau = 0.1$. The response of a membrane with $\tau = 0.1$ to monochromatic regular waves of frequency $\omega = 2.0\ \mathrm{rad\,s^{-1}}$ and $\omega = 2.4\ \mathrm{rad\,s^{-1}}$ is shown in Fig. 13. These figures can be contrasted against the response for materially undamped floating membrane, as was shown in Fig. 7 and Fig. 8. It is observed that for $\omega = 2.0\ \mathrm{rad\,s^{-1}}$, which lies between ω_1^w and ω_2^w, the damped membrane with $\tau = 0.1$ has a lower reflection coefficient of $K_R = 0.2968$ and lower transmission coefficient $K_T = 0.3911$, compared to $K_R = 0.3976$ and $K_T = 0.6025$ for $\tau = 0.0$. This is because a certain proportion of the wave energy is damped (or absorbed) by the membrane, computed as absorption coefficient $K_A = 0.3121$, using the Eq. (36d) for absorbed power P_A. A bigger contrast is observed for $\omega = 2.4\ \mathrm{rad\,s^{-1}}$. For this excitation frequency, which lies close to the wet natural frequency ω_2^w, we previously observed a nearly complete transmission of

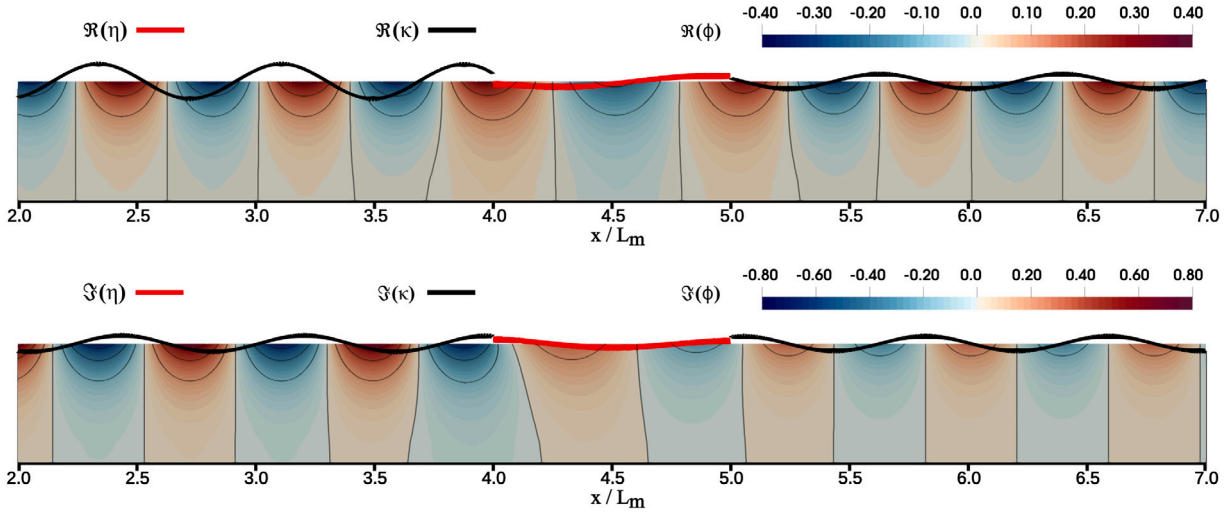

Fig. 12. Contour plot of solution of ϕ in the vicinity of the floating membrane, for $\omega = 2.0$ rad s^{-1} and $\tau = 0.10$. Exaggerated plots of the surface-elevation κ and membrane deflection η.

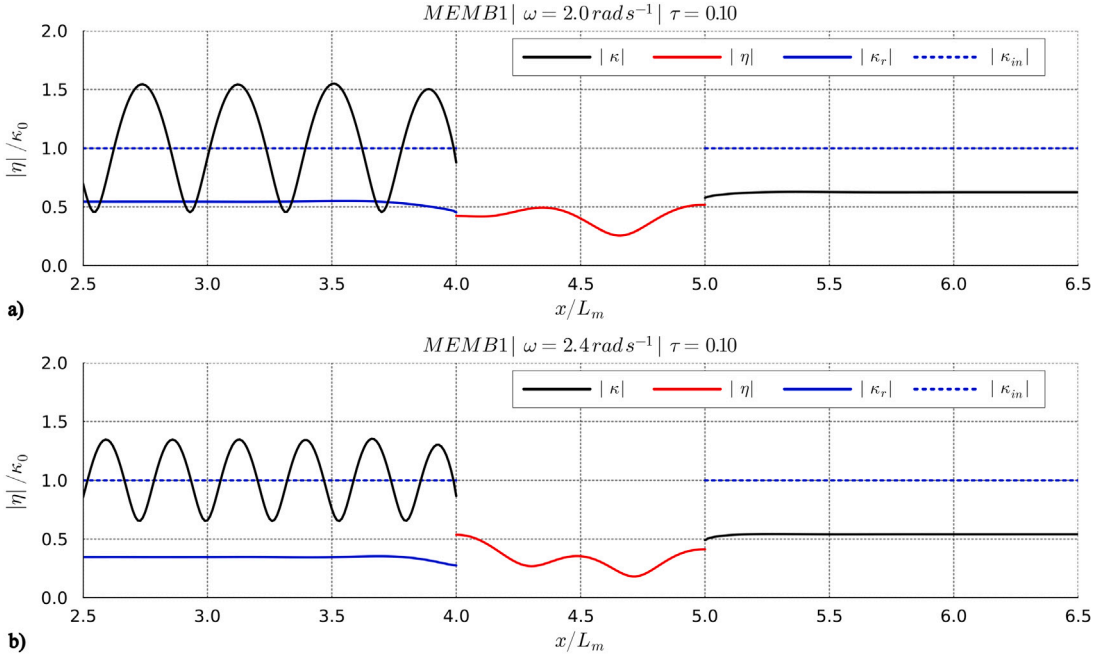

Fig. 13. Plots of magnitude of complex solution along the domain length for total free-surface elevation κ, membrane deflection η, reflected wave κ_r and incoming wave κ_{in}. (a) $\omega = 2.0$ rad s^{-1} and $\tau = 0.10$, (b) $\omega = 2.4$ rad s^{-1} and $\tau = 0.10$.

the incoming wave for $\tau = 0$. However, with $\tau = 0.1$ the wave is now partially reflected, with $K_R = 0.1203$ and $K_T = 0.2924$, and a relatively high absorption coefficient of $K_A = 0.5874$.

The same test is repeated for monochromatic waves in frequency range $\omega \in [0.7, 5]$ and for damping coefficients $\tau = \{0.01, 0.05, 0.10, 0.50\}$. The space varying solution for the magnitude of membrane deflection, reflected wave and transmitted wave are shown in Fig. 9b–d for values of $\tau = \{0.01, 0.05, 0.10\}$. The variation of reflection, transmission and absorption coefficients is plotted in Fig. 14. The wet natural frequencies ω_n^w of the membrane are also overlayed as arrows in Fig. 9b–d and vertical lines in Fig. 14. We observe that for the highest damping coefficient $\tau = 0.5$, the reflection and transmission coefficients monotonically increase and decrease with the wave frequency, respectively. For lower damping coefficients, the reflection coefficient plots have local minima and the transmission coefficient plots have local maxima at ω_n^w.

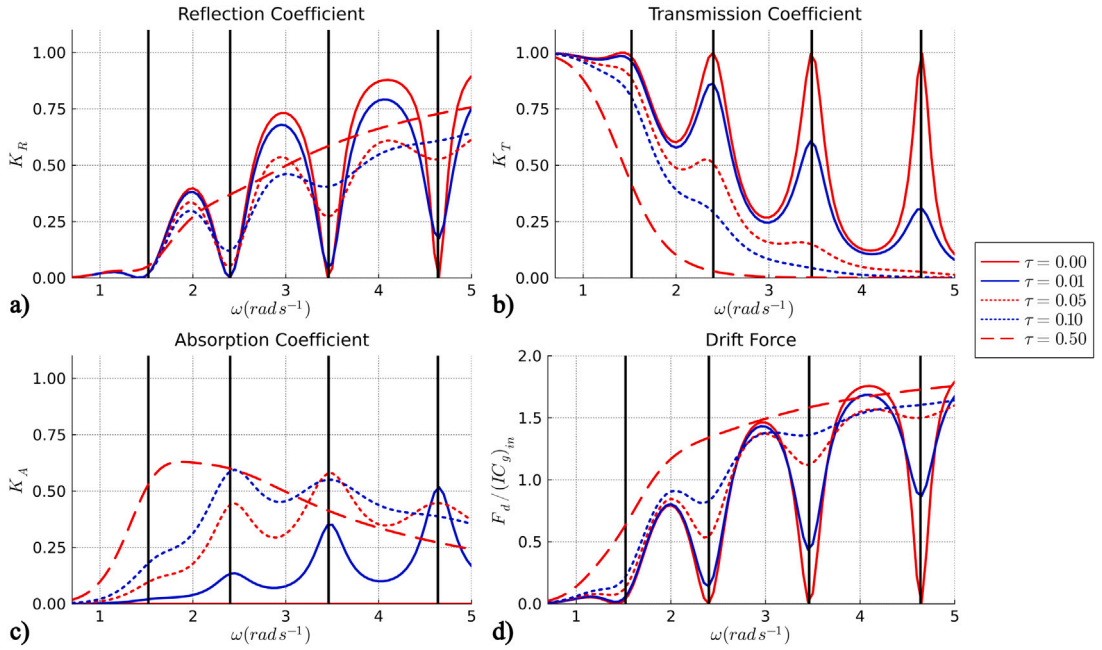

Fig. 14. Plots quantifying the (a) reflection coefficient, (b) transmission coefficient, (c) absorption coefficient and (d) drift force for floating membrane *MEMB1* across a range of frequencies. The results are plotted for various damping coefficients τ. The vertical lines are the wet natural frequencies of *MEMB1*.

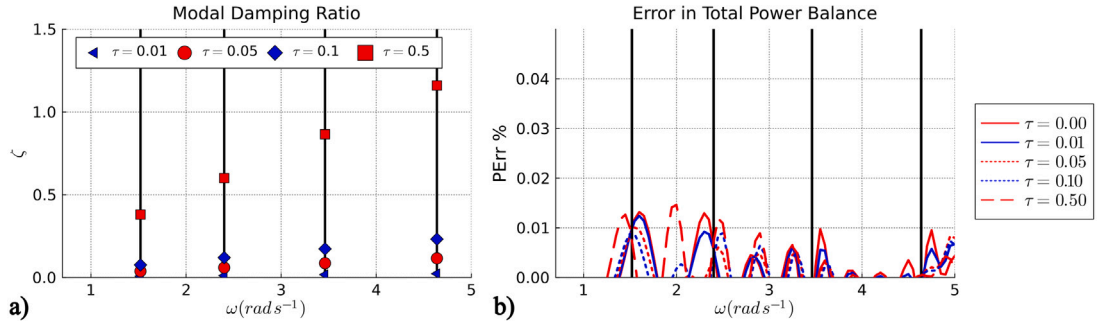

Fig. 15. Plots quantifying the (a) modal damping ratio, (b) error in power balance for floating membrane *MEMB1* across a range of frequencies. The results are plotted for various damping coefficients τ. The vertical lines are the wet natural frequencies of *MEMB1*.

We observe a rather interesting behaviour for the absorption coefficient K_A. In general, K_A has a local maxima at ω_n^w. However, the overall maxima of K_A is observed at different natural frequencies for different τ. For example, K_A is highest at ω_4^w for $\tau = 0.01$, while it is highest at ω_w^2 for $\tau = 0.10$. From Eq. (36d) it is evident that the absorbed power depends on the gradient of the deflection. The highest gradients are observed at higher wet modes. However, this is counterbalanced by the increasing reflection of the high-frequency waves by the membrane with higher τ. Therefore, the K_A increases for lower modes with increasing τ. This is a key result from the perspective of harvesting wave energy from membrane-type wave energy converters. It highlights that the material properties of the membrane can be "tuned" such that its wet natural frequencies align with peak wave frequencies of the ocean spectrum. This can in fact be done actively, either by controlling the tension of the membrane, or by varying the damping coefficient through the energy extraction mechanism.

We further emphasise the damping of the higher modes by the material damping using the plots of the modal damping ratio, presented in Fig. 15a. As shown in Eq. (6), the viscous damping in the material is proportional to the stiffness of the membrane. Therefore, the modal damping ratio is given by $\zeta = \frac{\tau\omega_n^w}{2}$. The drift force F_d acting on the floating membrane was estimated in Longuet-Higgins (1977) based on the conservation of momentum. The expression for F_d in constant water-depth h is given by Eq. (37a).

$$F_d = \frac{1}{4}\rho g\left(\kappa_{in}^2 + \kappa_r^2 - \kappa_t^2\right)\left(1 + \frac{2kh}{\sinh(2kh)}\right) = \frac{k}{\omega}C_g\,P_{in}\left(1 + K_R - K_T\right) \tag{37a}$$

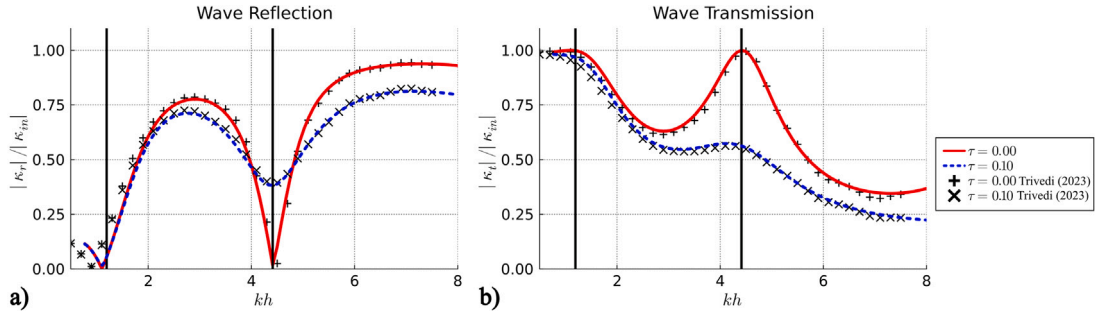

Fig. 16. Plots comparing the FE results from this manuscript with the BEM results from Trivedi and Koley (2022) for *MEMB1* with fixed edge boundary condition. (a) Wave reflection coefficient (b) Wave transmission coefficient. The results are plotted for $\tau = 0.0$ and $\tau = 0.10$. The vertical lines correspond to the wet natural frequencies of *MEMB1* with fixed-edge boundary condition.

$$(IC_g)_{in} = \frac{1}{4}\rho g \kappa_{in}^2 \left(1 + \frac{2kh}{\sinh(2kh)}\right) = \frac{k}{\omega} C_g P_{in} \tag{37b}$$

The variation of this drift force acting over a range of excitation frequencies ω for various values of τ is reported in Fig. 14d. Here the F_d is non-dimensionalised against the momentum flux of incoming wave $(IC_g)_{in}$ given by Eq. (37b). The expression for F_d highlights that higher wave reflection will increase the drift force on the floating body, whereas a higher wave transmission will reduce the drift force. Therefore, at the wet natural frequencies, the floating membrane will have $F_d = 0$, because the wave is completely transmitted for $\tau = 0$. The damping of the incoming wave by the viscoelastic membrane $\tau \neq 0$ will take out some incoming wave momentum. However, in general, this also increases the reflection and reduces the transmission of the wave as evident in Fig. 14a and Fig. 14b, especially for the higher frequencies. Therefore, F_d is generally observed to increase with higher τ.

The energy conservation properties of this monolithic formulation can be studied by comparing the reflection, transmitted and absorbed power Eqs. (36) against the input power of the incoming progressive wave. We quantify this energy conservation error as follows

$$\text{PErr} = \left(1 - \frac{P_R + P_T + P_A}{P_{in}}\right) \times 100 = \left(1 - K_R - K_A - K_T\right) \times 100 \tag{38}$$

Fig. 15b presents the plot of $PErr$ for all cases tested in Section 5.3.2. It should be noted that the error does not exceed 0.02% across the tested range of ω and τ, thereby affirming the effective conservation of total energy within the monolithic multi-physics model.

5.3.3. Comparison against contemporary literature: MEMB1 with fixed edge

There is limited literature available on the interaction of pre-tensioned floating membrane with free-surface waves. Most experiments conducted thus far have focused on thin-plate type problems. However, as explained in Section 2.2.1, the physics of pre-tensioned membrane differ from a thin-plate assumption. The work of Trivedi and Koley (2022) presents a Boundary Element Method (BEM) based analysis of the pre-tensioned floating membrane problem. In their methodology, the free-surface is defined using Green's function, where the wave number k is defined as the real and imaginary solutions of the dispersion relationship $\omega^2 = gk\tanh(kh)$.

Similar to Trivedi and Koley (2022), we consider a membrane of length $L_m = 2h$, $T_\rho/gL_m^2 = 0.025$, $m_\rho/L_m = 0.045$, floating in still-water depth $h = 10$ m. These properties are the same as the properties of *MEMB1* studied in the previous sections. However, while our previous analyses focused on *MEMB1* with free-edge boundary conditions, Trivedi and Koley (2022) investigated the membrane with fixed-edge boundary conditions. To facilitate a direct comparison with their findings, in this section, we examine *MEMB1* with fixed-edge boundary conditions, as defined by Eq. (7a).

We use the same numerical setup as described in Section 5.3.1. We subject the floating membrane to a range of wave frequencies. The initial test is conducted for $\tau = 0$. We monitor the amplitudes of the reflected wave $|\kappa_r|$ and transmitted wave $|\kappa_t|$. The study by Trivedi and Koley (2022) reported the wave reflection and transmission coefficients, defined as $|\kappa_r|/|\kappa_{in}|$ and $|\kappa_t|/|\kappa_{in}|$, respectively, as functions of kh. To facilitate comparison with their findings, we present the same quantities in Fig. 16. We repeat the tests for $\tau = 0.10$ and report the comparison against the results from Trivedi and Koley (2022).

Furthermore, following the natural frequency analysis outlined in Section 5.2, we compute the first four wet natural frequencies of *MEMB1* with fixed-edge boundary conditions. These wet natural frequencies are $\omega_{1-4}^{w} = \{0.9874, 2.0802, 3.1608, 4.3509\}$ rad s^{-1}, and are depicted as vertical lines at the corresponding kh values in Fig. 16.

The observations from the FE model results for *MEMB1* with fixed-edge boundary conditions closely resemble the observations for *MEMB1* with free-edge boundary condition, as detailed in Section 5.3.1 and Section 5.3.2. Once again, we note that for $\tau = 0$, the waves are nearly entirely transmitted at frequencies close to the computed wet natural frequency. Furthermore, the introduction of material damping, i.e., $\tau = 0.1$, results in increased reflection of higher wave frequencies.

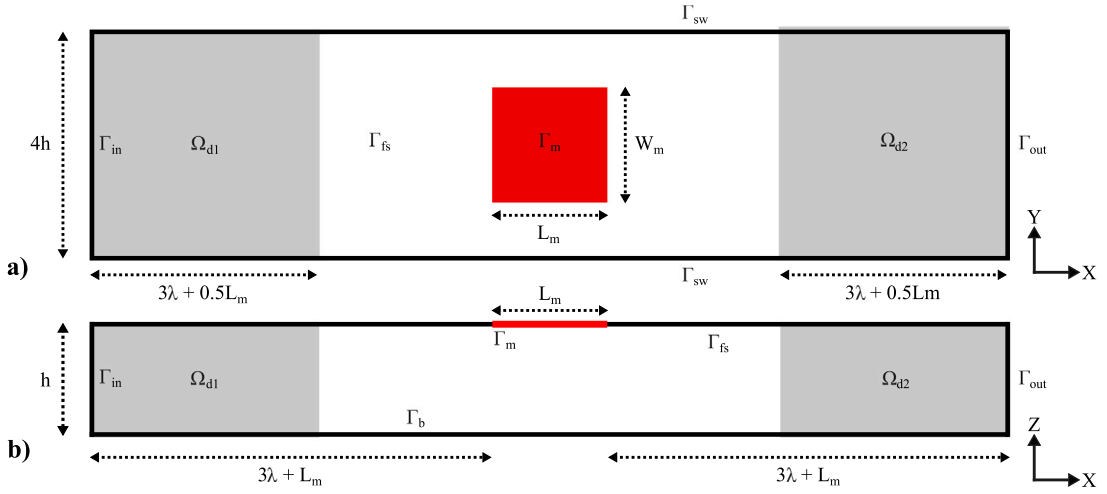

Fig. 17. Schematic of the numerical domain containing a viscoelastic floating membrane Γ_m (shown in red). (a) Top view of the domain. (b) Vertical view of the middle plane of the domain. (For interpretation of the references to colour in this figure legend, the reader is referred to the web version of this article.)

The results from the BEM analysis of Trivedi and Koley (2022) for these cases are presented as discrete points in Fig. 16. We observe similarities between the BEM results and the FE results for high frequencies. However, the results from BEM and FE differ at the low wave frequencies. In general, the BEM results indicate a higher reflection coefficient for the low wave frequencies compared to the FE results. Also, the BEM result indicates that the zero reflection happens at $kh = 0.88$, whereas the FE results indicate zero reflection at $kh = 1.11$. Moreover, for $\omega_1^w = 0.9874$, the corresponding $kh = 1.19$ aligns closely with the FE results. These observations suggest that the FE results correspond well with the computed wet natural frequency, while the BEM results tend to overestimate the reflection coefficient for low frequencies.

5.4. Natural frequencies of 2D finite floating membrane

The FEM formulation in Section 3.1 and the modal analysis in Section 4 can readily be applied to a 3D problem. Here the notation-based programming of *Gridap* FEM library and the operations-based logic of *Julia* programming language are particularly convenient for expanding the program to 3D with minimum modifications. In this section, we demonstrate the 3D capabilities of the model by analysing the natural frequencies and mode shapes of a 2D finite floating membrane and further study the interaction of this membrane with waves.

We conduct a modal analysis for a floating membrane *MEMB2D1*, with length and width $L_m = W_m = 2h$, uniform pre-tension $T_\rho/gL_m^2 = 0.025$, $m_\rho/L_m = 0.045$, floating in still-water depth of $h = 10$ m with free-edge boundary condition $\nabla\eta \cdot \mathbf{n} = 0$ on Λ_m. The modal analysis is done in a 3D cuboidal numerical domain of length $L_\Omega = 6h$, width $W_\Omega = 4h$ and depth h. Fig. 17 presents the schematic of the 3D problem, highlighting the boundaries of the domain. The side-wall boundaries Γ_{sw} and the bottom boundary Γ_b are all set to slip walls. This analysis does not require incoming waves. Therefore, the upstream and downstream boundaries Γ_{in} and Γ_{out} are both set to radiation boundary condition Eq. (29), and the domain does not have any damping zones. The membrane boundary Γ_m and the free-surface boundary Γ_{fs} are set to the same dynamic and kinematic boundary conditions specified in Eqs. (9). The domain is discretised into hexahedron elements, using uniform $\Delta x = 0.05L_m$ and $\Delta y = 0.05W_m$, while Δz varies exponentially from $\Delta z = 0.0408h$ near the free-surface to $\Delta z = 0.1280h$ near the bottom boundary, over 13 steps.

This configuration is solved to obtain the first 12 wet modes and natural frequencies of *MEMB2D1*, as shown in Fig. 18. We can contrast these with the mode shapes of the 1D membrane, as shown in Fig. 5 and Fig. 6. It is evident that the 2D mode shapes are a combination of the 1D shapes, along both the X and the Y axes. However, in this analysis, we constrained the Y-axis with wall boundary conditions. The asymmetry in the mode shapes is therefore observed due to the influence of the tank's side-walls.

5.5. Frequency domain solution of 2D finite floating membrane

We next examine the response of *MEMB2D1* having $\tau = 0$ for a range of wave frequencies. However, before delving into this analysis, it is crucial to understand the wave-celerity within the floating membrane. The dispersion relationship for the wave propagating in fluid free-surface is given by Eq. (39a). The dispersion relationship for a wave propagating through the floating membrane with $\tau = 0$ is given by Eq. (39b), where k_m and c_m are the wave-number and wave-celerity within the floating membrane. This equation is derived by combining the kinematic and dynamic boundary conditions on Γ_m in Eqs. (9). We refer the readers to Karmakar and Sahoo (2008) for the detailed derivation.

$$\omega^2 = gk\tanh(kh) \qquad \Longrightarrow \; c^2 = \frac{g}{k}\tanh(kh) \tag{39a}$$

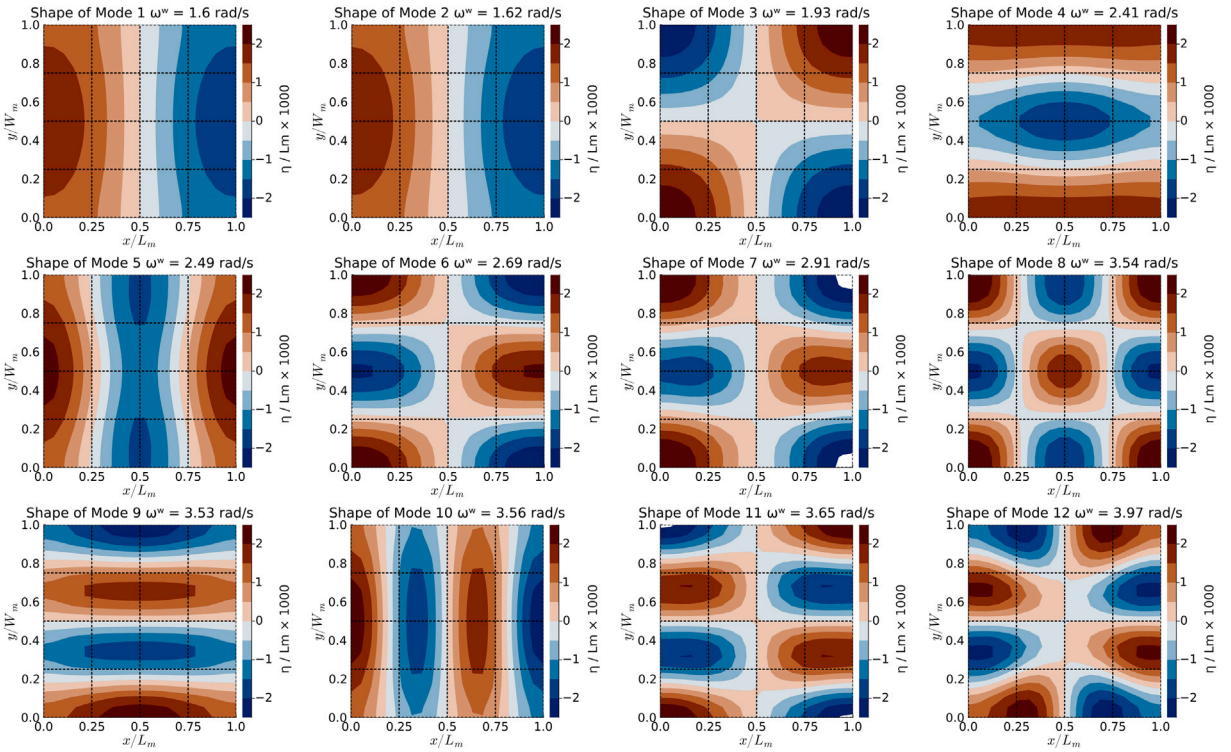

Fig. 18. Contour plots of mode shapes of first 12 wet modes for *MEMB2D1*, along with the corresponding natural frequencies ω^w.

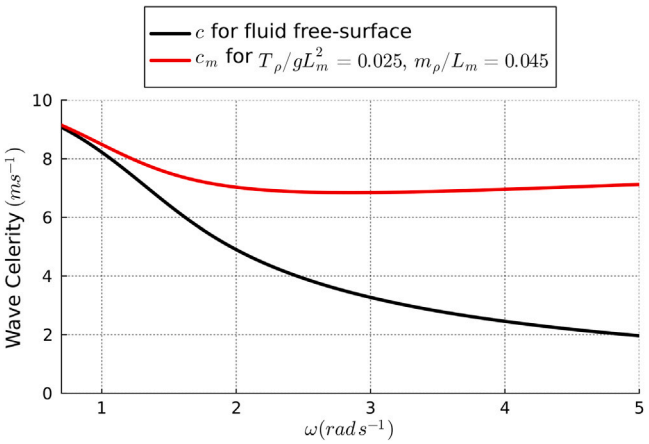

Fig. 19. Plots showing the comparison of wave celerity in floating membrane *MEMB2D1* vs the wave celerity in the fluid free-surface.

$$\omega^2 = gk_m \tanh(k_m h)\left(1 - \frac{m}{\rho g}\omega^2 + \frac{T}{\rho g}k_m^2\right) \qquad \Longrightarrow \quad c_m^2 = \frac{g}{k_m}\tanh(k_m h)\left(1 - \frac{m}{\rho g}\omega^2 + \frac{T}{\rho g}k_m^2\right) \tag{39b}$$

The comparison of wave celerity c_m for *MEMB2D1* and c for fluid is shown in Fig. 19. This comparison reveals that the wave celerity, and consequently the wavelength, is greater for the wave travelling within the membrane in contrast to the free surface of the fluid. As per the conclusions of Zhang and Schreier (2022), this should result in the spreading of the waves downstream of *MEMB2D1*.

We analyse the response of *MEMB2D1* for wave-frequencies $\omega \in [1.5, 4.5]$ rad s^{-1}, corresponding to wave-length $\lambda/L_m \in (0.15, 1.3)$. The schematic of the numerical domain used for this analysis is shown in Fig. 17. Similar to Section 5.4, the numerical domain has a width $W_\Omega = 4h$ and depth h. The length of the domain is set as $L_\Omega = 6\lambda + 2L_m$, including two damping zones Ω_{d1} in $x \in (-3\lambda - 0.5L_m, -0.5L_m)$ upstream and Ω_{d2} in $x \in (1.5L_m, 1.5L_m + 3\lambda)$ downstream of the membrane, each of length 3λ to efficiently absorb the reflected waves. The membrane is placed in the middle of the domain's free-surface between $x \in (0, 1L_m)$

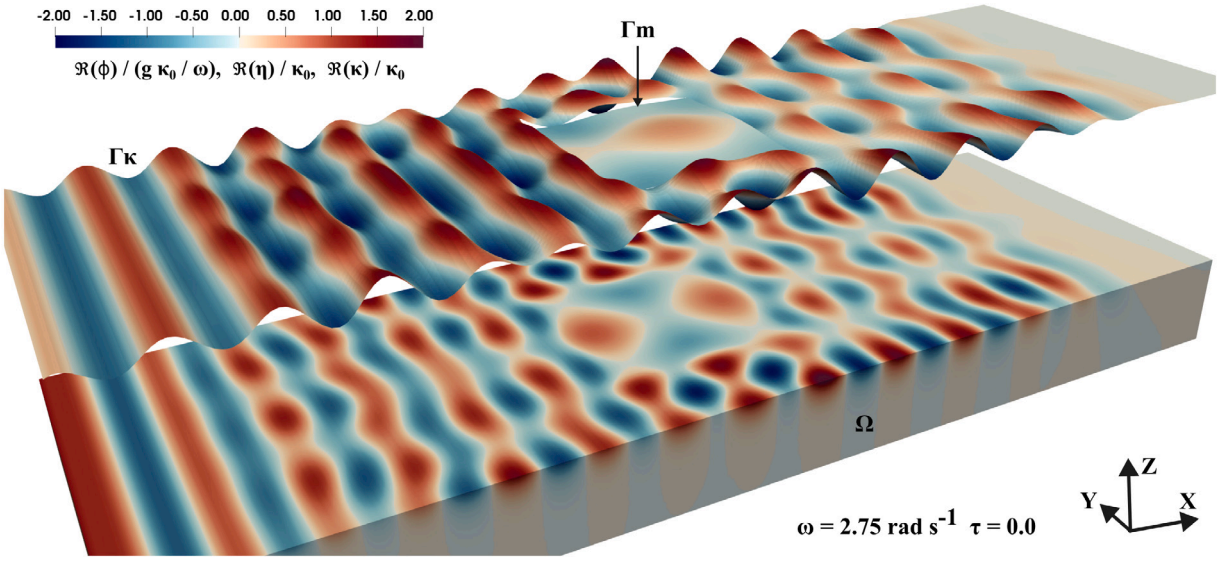

Fig. 20. 3D render of the solution for $\Re(\phi)$ on Ω, $\Re(\eta)$ on Γ_m and $\Re(\kappa)$ on Γ_κ, throughout the numerical domain, for $\omega = 2.75$ rad s^{-1} and $\tau = 0.0$.

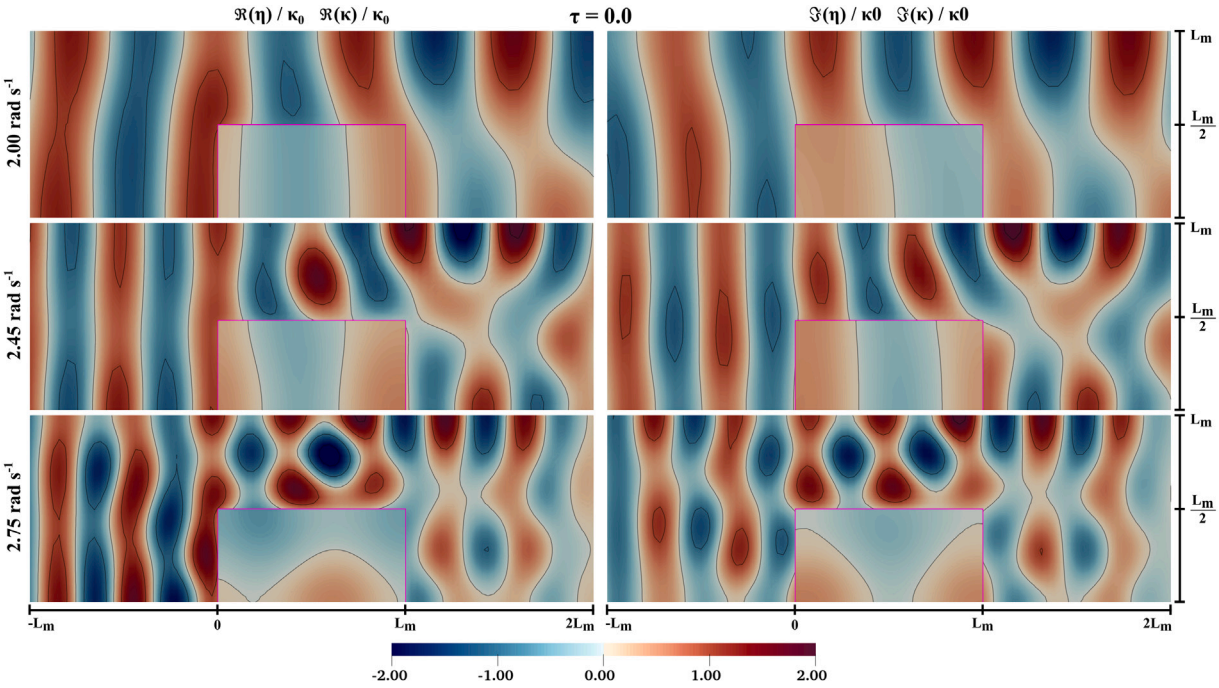

Fig. 21. Contour plots of the spatial variation of the solution of membrane deflection η and surface elevation κ in the vicinity of the membrane for $\omega = \{2.00, 2.45, 2.75\}$ rad s^{-1} and $\tau = 0.0$.

and $y \in (-0.5W_m, 0.5W_m)$. The domain is meshed using second-order hexahedron elements, having $\Delta x = \lambda/12$, $\Delta y = \lambda/12$ and Δz varying exponentially from $0.0385h$ near the free-surface to $0.1988h$ near the bottom boundary over 10 steps. Given that the wave-length is expected to be longer within the membrane compared to the fluid free-surface, the mesh size is governed by the wave-length within the fluid free-surface.

The analysis is first done for materially undamped membrane having $\tau = 0.0$. Fig. 20 presents a 3D view of the complete numerical domain for $\omega = 2.75$ rad s^{-1}, highlighting the complex interaction of the incoming waves with the 2D membrane and the tank side-walls. The damping zones Ω_{d1} and Ω_{d2} upstream and downstream of the domain are observed to absorb the waves scattered by the membrane. Subsequently, we narrow our focus to the vicinity of the membrane. Fig. 21 presents the real and

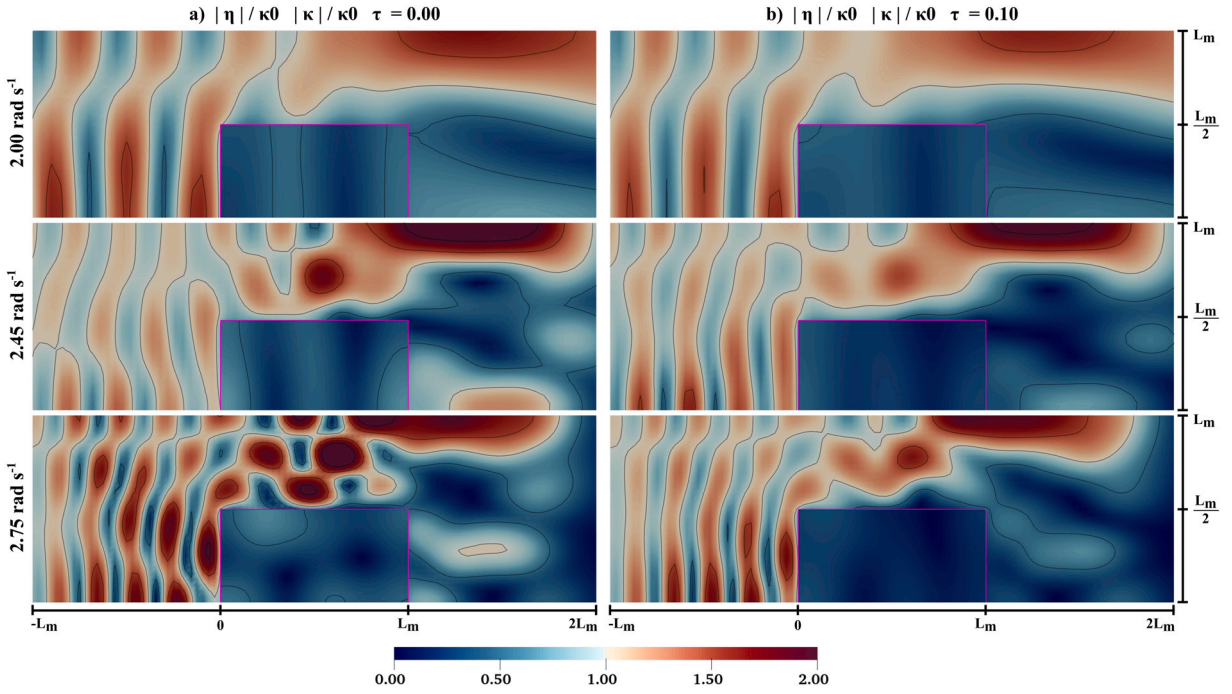

Fig. 22. Contour plots showing the spatial variation of the absolute value of the solution of membrane deflection η and surface elevation κ in the vicinity of the membrane for $\omega = \{2.00, 2.45, 2.75\}$ rad s^{-1} and $\tau = \{0.0, 0.10\}$.

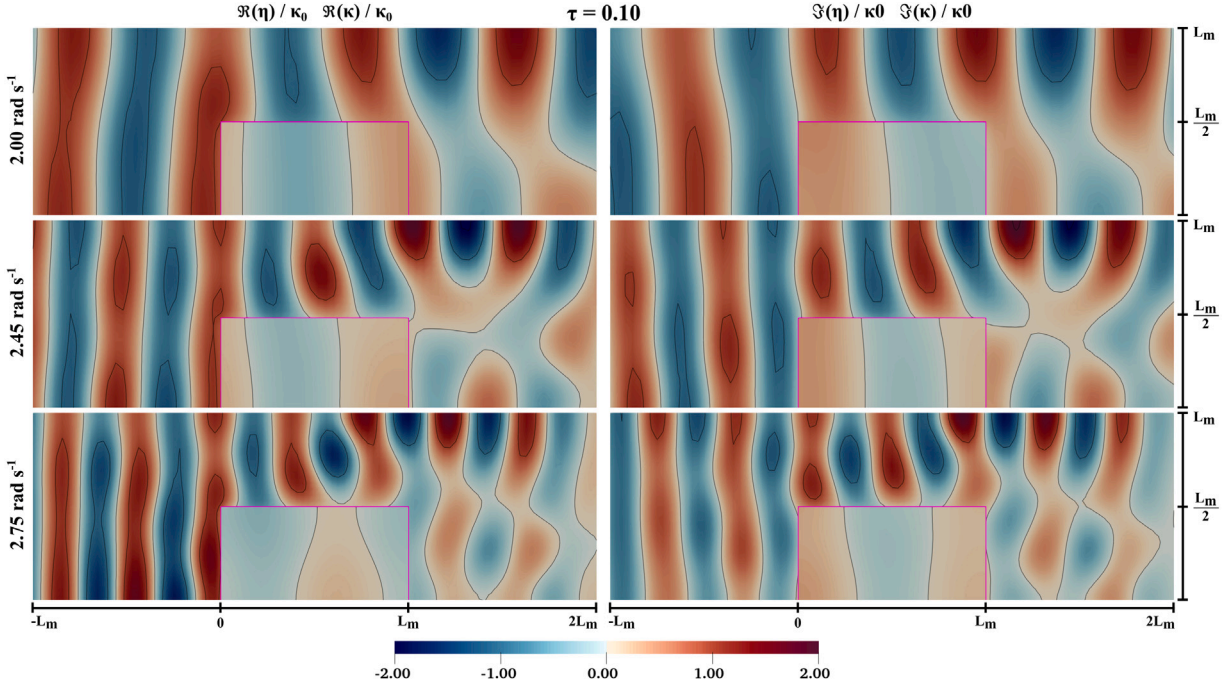

Fig. 23. Contour plots of the spatial variation of the solution of membrane deflection η and surface elevation κ in the vicinity of the membrane for $\omega = \{2.00, 2.45, 2.75\}$ rad s^{-1} and $\tau = 0.10$.

imaginary value of the solution for surface elevation κ and membrane deflection η, scaled against the input wave amplitude κ_0 for three different ω. Fig. 22a presents the absolute value of the solution for $\tau = 0.0$. We use these figures to conduct a qualitative assessment of the hydro-elastic interaction between the 2D membrane and the waves. These figures highlight comparatively longer

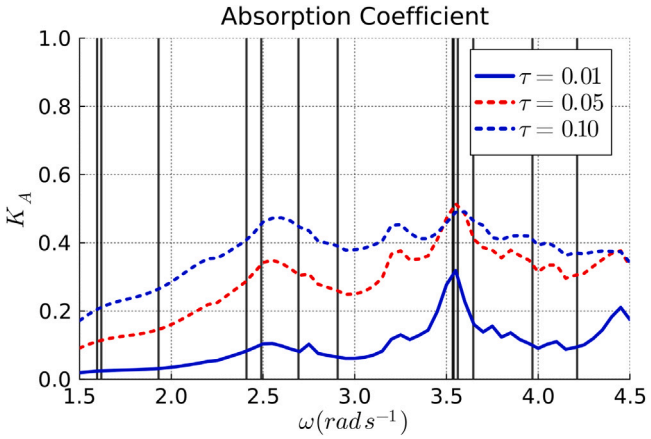

Fig. 24. Plots of absorption coefficient for *MEMB2D1* for a range of excitation frequencies and $\tau = \{0.01, 0.05, 0.10\}$. Here the vertical lines denote the wet natural frequencies of the 2D finite floating membrane.

wave-length within the membrane contrasted against the wave-length within the free-surface. This relative acceleration of the wave within the membrane along with the diffraction of the wave by the boundary of the membrane creates a complex outward dispersion of the transmitted wave. This effect is particularly emphasised by the reflection of the transmitted wave against the tank side-walls and the creation of a sheltered zone in the wake of the membrane. Further, Fig. 22a indicates that reflection from the membrane is more pronounced for high frequencies, as evident from the higher peaks upstream of the membrane for $\omega = 2.75\ \mathrm{rad\,s^{-1}}$ compared to $\omega = 2.0\ \mathrm{rad\,s^{-1}}$. At $\omega = 2.45\ \mathrm{rad\,s^{-1}}$, which is close to the wet natural frequency $\omega_5^w = 2.49\ \mathrm{rad\,s^{-1}}$, we observe a lower reflection of the wave as evident from lower peaks in the upstream solution in Fig. 22a. In fact the real value of the deflection η for $\omega = 2.45\ \mathrm{rad\,s^{-1}}$ closely aligns with the real value of the mode shape ω_5^w presented in Fig. 18.

Similar to Section 5.3, we repeat the analysis for different values of damping coefficient τ. Fig. 23 presents real and imaginary values of the solutions for the membrane deflection and free-surface elevation in the vicinity of the membrane for $\tau = 0.10$. Fig. 22b presents the absolute value of the solution for $\tau = 0.10$. Fig. 22 distinctly highlights the lower magnitude of the free-surface elevation and membrane deflection for $\tau = 0.10$ compared to $\tau = 0.0$, primarily due to partial absorption of the incoming wave energy by the membrane. The 2D membrane essentially can absorb energy from deformation along both the X and Y axes. This absorbed energy can be quantified using Eq. (36d). Fig. 24 presents the plots of absorption coefficient K_A for a range of frequencies for $\tau = \{0.01, 0.05, 0.10\}$. We observe irregularities in the K_A plot for $\tau = 0.01$, potentially influenced by the presence of tank side-walls. For higher damping ratio τ, these irregularities in the K_A plot are smoothed out. The plot also marks the computed wet natural frequencies of *MEMB2D1*. We once again observe a local peak at a few, not all, wet natural frequencies of the membrane. This is potentially because the membrane was excited by unidirectional waves propagating along the length of the membrane, which only excited a few of the wet modes. Nevertheless, the analysis underscores that upon identifying the predominant wet modes, it becomes feasible to devise mechanisms aimed at harnessing the maximum potential offered by these modes.

5.6. Application to 2D floating membrane around a monopile

In this section, we present the application of the developed model to a physical problem. We study the interaction of a bottom-fixed monopile foundation with a circular viscoelastic membrane in the presence of ocean waves. The viscoelastic membrane here can be installed as a floating breakwater to offset/partially reflect the ocean waves and thereby protect the monopile foundation. It can also function as a wave-energy converter, extracting ocean energy from a wide bandwidth of frequencies, thus exploring the synergy between different ocean renewable technologies.

We consider the typical dimensions of the wind-turbine foundation installed in the North Hoyle wind farm, located in Liverpool Bay, 8 km off the coast of North Wales. These monopile foundations have a diameter 4m and are installed in the depth of 7 – 11 m. We place this monopile on a submerged conical island, in order to show the capabilities of the model to simulate irregular sea-bed. The specifics of the test case are shown in Fig. 25. A monopile of diameter $D_c = 4$ m and length $L_c = 1.5D_c$ is placed in the middle of a numerical domain with width $W_\Omega/D_c = 10$, length $L_\Omega/D_c = 40$ and depth $h = 10$ m. The monopile is placed on top of a conical island with top diameter $3D_c$, bottom diameter $5D_c$ and height $0.4h$. The monopile is surrounded by a viscoelastic floating membrane Γ_m of diameter $D_m = 6D_c$. The membrane is made of high-density polyethylene (HDPE), having density of $\rho_m = 970\ \mathrm{km^3}$ and thickness of $h_m = 0.005$ m, resulting in $m_\rho/D_m = 2.08 \times 10^{-4}$, and has a pre-tension of $T_\rho/gD_m^2 = 8.633 \times 10^{-3}$.

The boundary condition for the side-walls Γ_{sw}, cylinder boundary Γ_{cyl} and the bottom Γ_b are slip walls. Additionally, the domain has two damping zones, each of length $L_d/D_C = 10$, attached to the inlet Γ_{in} and outlet Γ_{out} boundaries to absorb the waves dispersed by the membrane and the monopile. The domain is decomposed using an unstructured mesh of second-order tetrahedral elements. The element size Δr is prescribed as $\Delta r/D_c = 0.15$ at the top boundary $\Gamma_m \cup \Gamma_{fs}$ and at the monopile boundary Γ_{cyl}. For the

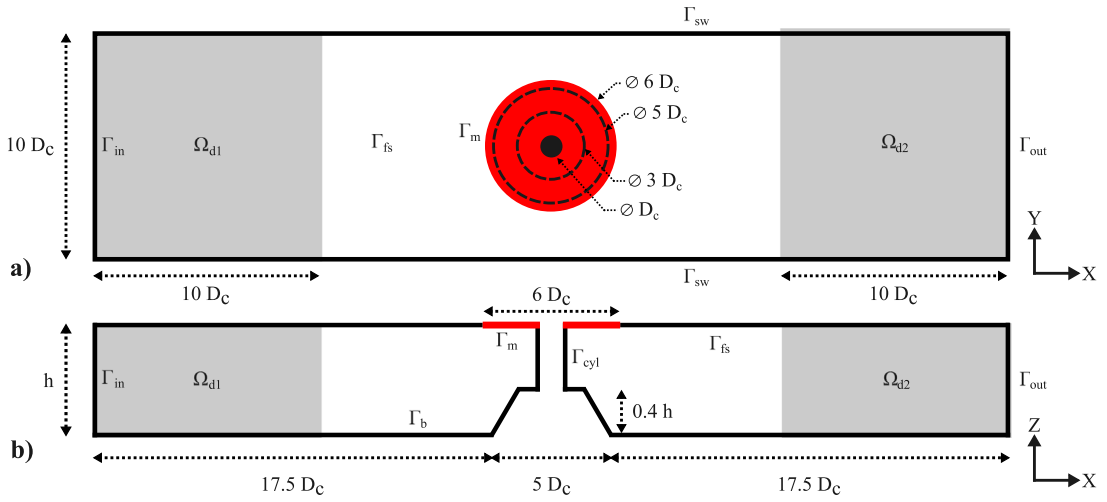

Fig. 25. Schematic of the numerical domain containing a monopile with boundary Γ_{cyl}, surrounded by a viscoelastic floating membrane Γ_m (shown in red). The monopile is installed on a conical submerged island. (a) Top view of the domain. (b) Vertical view of the middle plane of the domain. (For interpretation of the references to colour in this figure legend, the reader is referred to the web version of this article.)

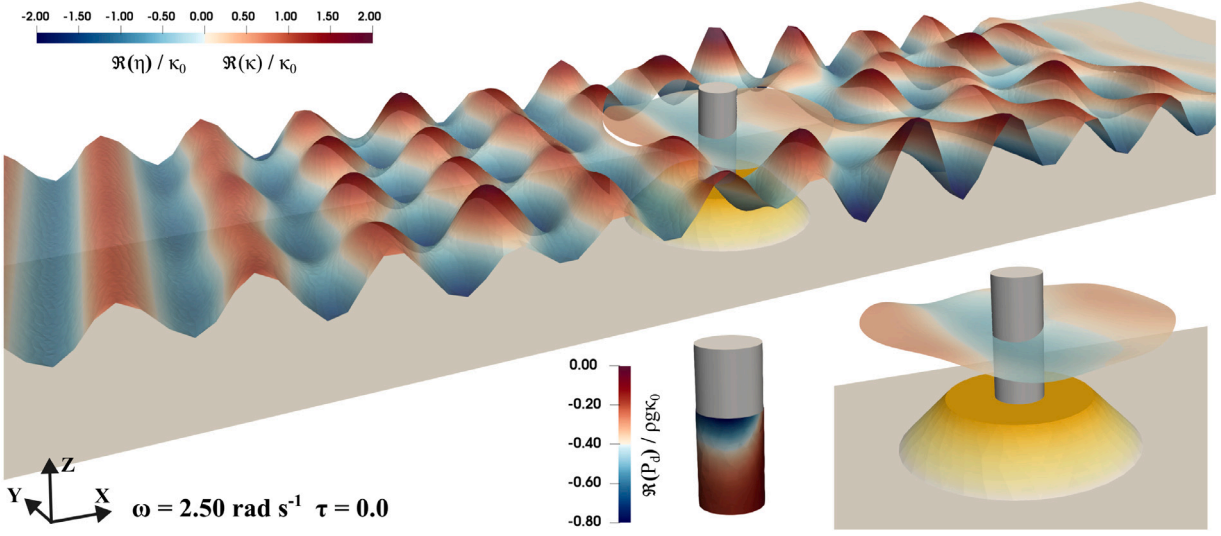

Fig. 26. 3D render of the solution for $\Re(\eta)$ and $\Re(\kappa)$ throughout the numerical domain for $\omega = 2.50$ rad s^{-1} and $\tau = 0.0$. The figure also includes a zoomed-in view of the membrane deflection around the monopile and the contour plot of the corresponding dynamic pressure $\Re(P_d)$ on the monopile surface.

remaining domain, the element size is controlled using an exponential background field function gradually varying the mesh size from $\Delta r/D_c = 0.15$ on the top to $\Delta r/D_c = 0.50$ at the bottom, resulting in 551,433 s order tetrahedral elements. These simulations are executed as a serial process on a system with Intel(R) Xeon(TM) E5-6248R processor and 192 GB of RAM. The run-time for simulations is 5 min per frequency.

The membrane and monopile are exposed to a range of excitation frequencies $\omega \in [1.5, 3.2]$ rad s^{-1}. For this range of frequencies, $D_c/\lambda \in (0.2, 0.8)$, and hence there is significant diffraction of the waves by the monopile. Fig. 26 presents a 3D render of the solution for the membrane deflection and the free-surface elevation over the complete numerical domain for $\omega = 2.5$ rad s^{-1} and $\tau = 0.0$. It also highlights the performance of the damping zones upstream and downstream of the monopile. The solution for velocity potential ϕ can be used for evaluating the dynamic pressure P_d in the domain, $P_d = \rho i\omega\phi$. Fig. 26 additionally presents a contour plot of the dynamic pressure on the monopile due to the action of the wave for the corresponding scenario. Using this dynamic pressure, we evaluate the dynamic force on the monopile due to the action of the waves $\mathbf{F} = \int_{\Gamma_{cyl}} P_d\, \mathbf{n}_{cyl}\, d\Gamma$. This force is used to evaluate the performance of the viscoelastic membrane in sheltering the monopile foundation from the ocean waves. Fig. 27a presents the magnitude of the dynamic force acting along the wave direction (X-axis) on the monopile due to the action of the waves. Here the calculated force F_x is appropriately non-dimensionalised as $F_{x,nd}$, considering the volume of the cylinder, the wave-elevation

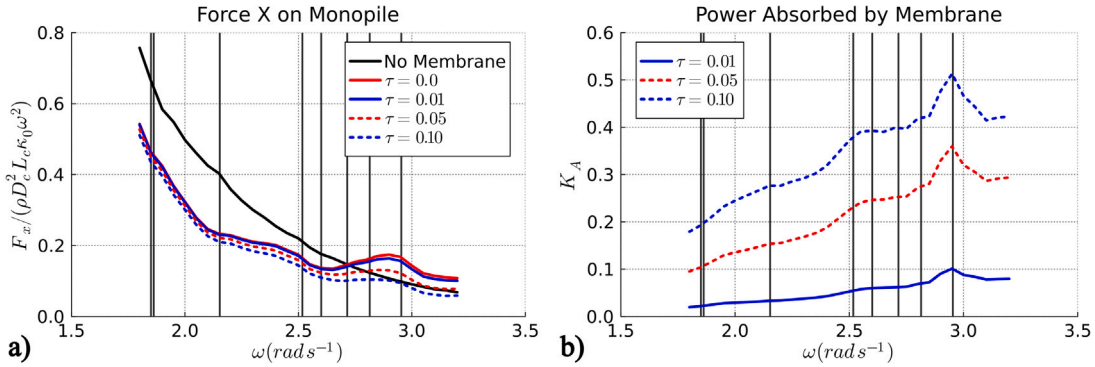

Fig. 27. (a) Plots of wave force on the monopile, in the absence and presence of the viscoelastic floating membrane, for a range of wave frequencies and various damping coefficients τ. (b) Plots of wave power absorbed by the viscoelastic membrane, for a range of wave frequencies and various damping coefficients. The vertical lines in the plot are the wet natural frequencies of the floating membrane.

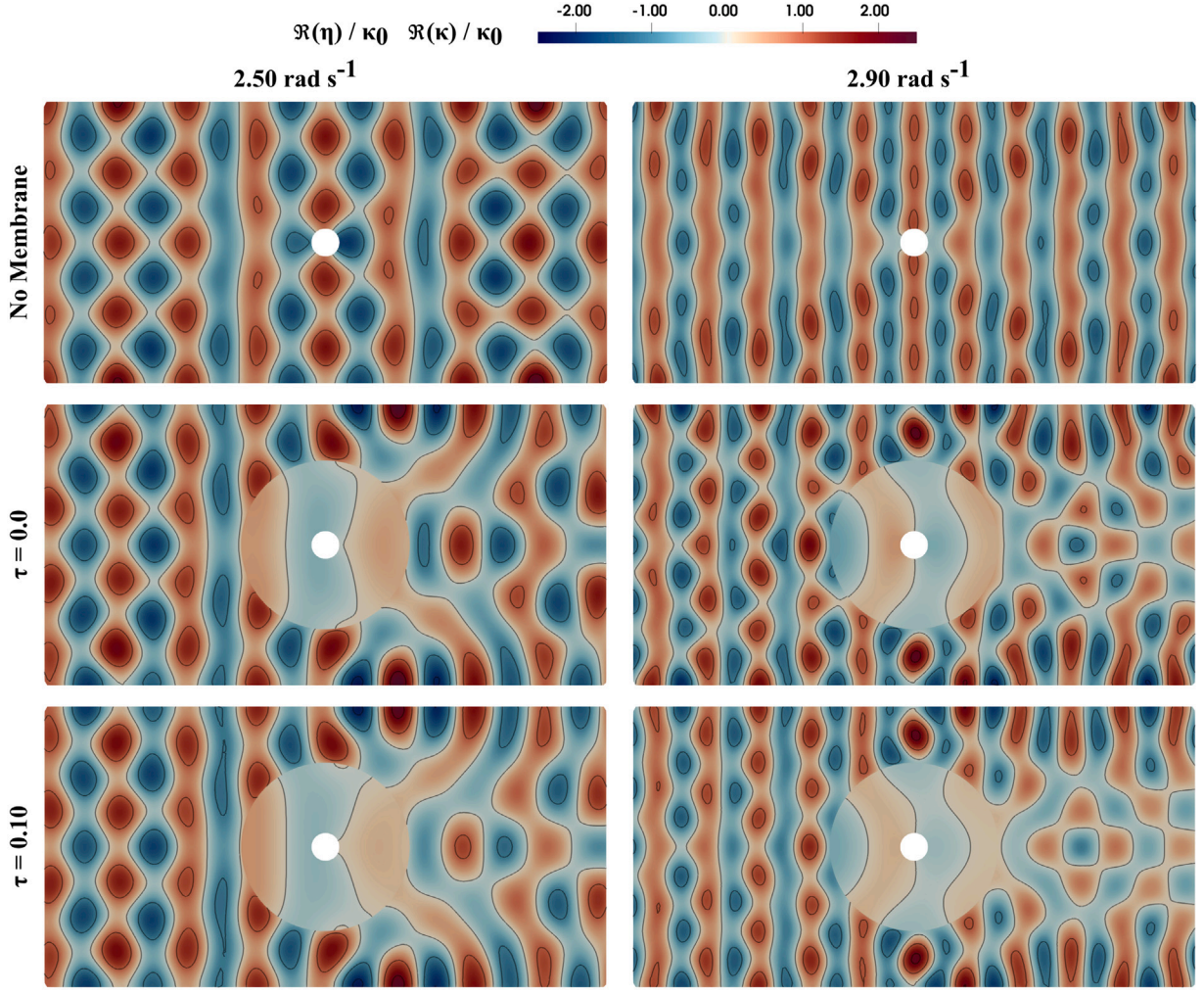

Fig. 28. Contour plots showing the spatial variation of $\Re(\eta)$ and $\Re(\kappa)$ in the vicinity of the monopile for $\omega = \{2.50, 2.90\}$ rad s^{-1}. The figures present results in the absence of the floating membrane, and in the presence of the floating membrane with $\tau = 0.0$ and $\tau = 0.10$.

and the wave-frequency. Additionally, Fig. 27b presents the wave power absorbed/dissipated by the viscoelastic membrane having $\tau \neq 0.0$.

In the absence of a surrounding membrane, the force ($F_{x,nd}$) acting on the monopile follows a steadily decreasing pattern as the wave frequency increases. When the thin viscoelastic membrane is introduced, there is a noticeable reduction in wave force, particularly at lower wave frequencies. The reason for this can be deduced from the contour plots of membrane deflection and wave elevation in the vicinity of the membrane, as shown in Fig. 28. The viscoelastic membrane partially reflects the incoming waves, as was discussed in Section 5.3. Additionally, the higher wave celerity within the membrane, compared to the fluid free-surface $c_m > c$ (see Fig. 19), causes outward dispersion of the incoming waves. The higher c_m is distinctly evident in the longer wavelength within the membrane in Fig. 28. These combined effects contribute to a reduction in the wave force acting on the monopile.

However, Fig. 27a shows an increase in wave force in the presence of the membrane beyond $\omega = 2.7\ \mathrm{rad\,s^{-1}}$, peaking around $\omega = 2.9\ \mathrm{rad\,s^{-1}}$. This increase is attributed to the existence of membrane mode at $\omega = 2.9\ \mathrm{rad\,s^{-1}}$, highlighted by the vertical lines in the plot. The excitation of this mode leads to resonance and consequently, an increase in the force acting on the monopile in the presence of the membrane. The introduction of viscous damping ($\tau \neq 0$) can partially mitigate this effect, as evident from the plot for $\tau = 0.10$ in Fig. 27a. The plot of absorption coefficient K_A for $\tau \neq 0$ once again reveals local peaks at a few wet natural frequencies of the membrane in Fig. 27b, consistent with our observations in the earlier sections.

6. Conclusions

In this manuscript, we have presented a monolithic finite-element model that couples linear free-surface potential flow with the viscoelastic membrane equation. The study has rigorously defined the coupled multi-physics problem, along with the necessary boundary conditions. Subsequently, the manuscript presented the weak form of the system, and established the consistency and energy-conserving properties of the system. Furthermore, the weak form was used as the basis for deriving the wet modal analysis for the coupled system, along with the description of the iterative algorithm for calculating the wet natural frequencies of the floating membrane.

Subsequently, the manuscript illustrates the convergence characteristics of the model, obtaining an $O(r+1)$ rate of convergence for elements of polynomial degree of r. Following this, we focus on the wet natural frequencies and corresponding mode shapes of a 1D floating membrane, and study their variation with respect to the tension and the mass of the membrane. The manuscript underscores the dominance of added mass, evident in the lower values of wet natural frequency in comparison to the dry natural frequency. Furthermore, it emphasises the primary dependence of the wet natural frequency on the membrane tension.

The manuscript further examines the interaction of 1D floating membrane with incoming ocean waves. We first study the behaviour of the materially undamped membrane with $\tau = 0$, employing reflection and transmission coefficients. In general, we observed the reflection coefficient to increase with the wave frequency. Crucially, the floating membrane here is observed to function akin to a mechanical filter, where the waves at the wet natural frequency of the membrane are found to be entirely transmitted. This underscores the significance of computing these frequencies and presents the mechanism for tuning the response of the floating membrane. Subsequently, the manuscript studies materially damped membranes having $\tau \neq 0$. Here we additionally calculate the wave energy absorbed by the membrane, indicative of energy harvested by a wave-energy converter or the energy dissipated by a floating breakwater or floating solar platform. We also report the drift force on the membrane, calculated based on the conservation of momentum. At lower low frequencies, the membrane predominantly exhibits heaving motion. For higher frequencies, the membrane largely reflects the waves, with minimal deflection response. Hence there is a narrow bandwidth of the frequencies, depending on the value of τ, which induces an elastic response from the membrane. At the wet natural frequencies, we observe local peaks in the absorption and transmission coefficients and local troughs in reflection and drift force. The specific global peak in absorption coefficient is dependent on the value of τ.

The following sections study the 3D problem of a 2D finite floating membrane, underscoring the versatility of the developed model and wet modal analysis. We first study a square membrane and report its calculated wet natural frequencies and mode shapes. Subsequently, we examine the interaction of this finite 2D membrane with ocean waves for a wide range of frequencies. We demonstrate that the wavelength within the membrane is longer than within the free surface, aligning with the membrane's dispersion relationship. This leads to an outward dispersion of the wave and creates a sheltered zone in the wake. Other observations for 2D membranes were similar to the 1D case, with local peaks in absorption coefficient at certain natural frequencies and increased reflection of higher frequency waves. The final numerical test studies the interaction of a circular floating membrane with a monopile, assessing its efficacy as a floating breakwater. In this scenario, the membrane is noted to decrease the wave force on the monopile at lower frequencies. However, our analysis underscores that the excitation of the wet mode of the membrane can, in fact, amplify the wave force on the membrane.

The manuscript has presented the formulation and capabilities of this monolithic FE model for studying irregularly shaped 2D visco-elastic membranes in 3D fluid environments. The presented FE model adeptly captures both propagating and evanescent modes of waves generated in the fluid domain as a result of the elastic response of the floating membrane. This capability sets it apart from the traditional mode expansion approach, which may have limitations in analysing evanescent modes, if any. Such analysis is particularly crucial for low-frequency excitation, as emphasised in Section 5.3.3. Lastly, our results underscore the promising potential of low-dimensional (thin) structures to serve as effective wave-energy converters or breakwaters, leveraging material damping to enhance their performance.

The presented model can hence be used for the structural analysis of floating membranes for floating solar, floating breakwater and wave-energy converter applications. Our subsequent work will focus on implementing nonlinear free-surface and nonlinear membrane deflection governing equations. The presented FE model can readily accommodate nonlinear free-surface dynamics through a semi-Lagrangian approach. A significant challenge ahead is determining the value of τ. The current work has demonstrated

the impact of this coefficient on the membrane response. Furthermore, the model can accommodate the variation in τ based on the membrane and the excitation frequency. However, there is little information in the literature about calculating this coefficient for various materials. Additionally, in the content of wave-energy converters, additional research is needed for correlating the damping coefficient with the electro-mechanical process of converting deformation to electrical energy.

CRediT authorship contribution statement

Shagun Agarwal: Writing – original draft, Visualization, Validation, Software, Methodology, Formal analysis. **Oriol Colomés:** Writing – original draft, Supervision, Methodology, Funding acquisition, Conceptualization. **Andrei V. Metrikine:** Writing – review & editing, Supervision.

Declaration of competing interest

The authors declare that they have no known competing financial interests or personal relationships that could have appeared to influence the work reported in this paper.

Data availability

Data will be made available on request.

Acknowledgements

This research was supported by the Dutch Research Council (NWO) grant number *OCENW.XS22.1.051*.

References

Akkerman, I., Meijer, J., Eikelder, M.T., 2020. Isogeometric analysis of linear free-surface potential flow. Ocean Eng. 201, 107114. http://dx.doi.org/10.1016/j.oceaneng.2020.107114.

Badia, S., Verdugo, F., 2020. Gridap: An extensible Finite Element toolbox in Julia. J. Open Source Softw. 5 (52), 2520. http://dx.doi.org/10.21105/joss.02520.

Berstad, A., Grøn, P., 2023. Model basin testing of a floating solar PV plant compared to analysis. In: 10th Conference on Computational Methods in Marine Engineering. CIMNE, http://dx.doi.org/10.23967/marine.2023.094.

Bezanson, J., Edelman, A., Karpinski, S., Shah, V.B., 2017. Julia: A fresh approach to numerical computing. SIAM Rev. 59 (1), 65–98. http://dx.doi.org/10.1137/141000671.

Boren, B., 2021. Distributed embedded energy converters for ocean wave energy harvesting: Enabling a domain of transformative technologies: Preprint. Renew. Energy 9, URL https://www.osti.gov/biblio/1822178.

Cazzaniga, R., Rosa-Clot, M., 2021. The booming of floating PV. Sol. Energy 219, 3–10. http://dx.doi.org/10.1016/j.solener.2020.09.057.

Cho, I.H., Kim, M.H., 1998. Interactions of a horizontal flexible membrane with oblique incident waves. J. Fluid Mech. 367, 139–161. http://dx.doi.org/10.1017/S0022112098001499.

Collins, I., Hossain, M., Dettmer, W., Masters, I., 2021. Flexible membrane structures for wave energy harvesting: A review of the developments, materials and computational modelling approaches. Renew. Sustain. Energy Rev. 151, 111478. http://dx.doi.org/10.1016/j.rser.2021.111478.

Colomés, O., Verdugo, F., Akkerman, I., 2022. A monolithic finite element formulation for the hydroelastic analysis of very large floating structures. Internat. J. Numer. Methods Engrg. nme.7140. http://dx.doi.org/10.1002/nme.7140.

Colomes Gene, O., 2022. Code Used to Generate the Data Underlying the Publication: A Monolithic Finite element Formulation for the Hydroelastic Analysis of Very large floating structures. 4TU.ResearchData, http://dx.doi.org/10.4121/19601419.

Dean, R.G., Dalrymple, R.A., 1991. Water wave mechanics for engineers and scientists. In: Advanced Series on Ocean Engineering, vol. 2, World Scientific Publishing Co. Pte. Ltd., http://dx.doi.org/10.1142/9789812385512.

Guo, Y., Mohapatra, S., Guedes Soares, C., 2022. Submerged breakwater of a flexible porous membrane with a vertical flexible porous wall over variable bottom topography. Ocean Eng. 243, 109989. http://dx.doi.org/10.1016/j.oceaneng.2021.109989.

Humamoto, T., Fujita, K., 2002. Wet-mode superposition for evaluating the hydroelastic response of floating structures with arbitrary shape. In: ISOPE International Ocean and Polar Engineering Conference. ISOPE–I, ISOPE.

Kargar, S.M., Hao, G., 2022. An atlas of piezoelectric energy harvesters in oceanic applications. Sensors 22 (5), 1949. http://dx.doi.org/10.3390/s22051949.

Karmakar, D., Sahoo, T., 2008. Gravity wave interaction with floating membrane due to abrupt change in water depth. Ocean Eng. 35 (7), 598–615. http://dx.doi.org/10.1016/j.oceaneng.2008.01.009.

Kashiwagi, M., 1998. A B-spline Galerkin scheme for calculating the hydroelastic response of a very large floating structure in waves. J. Mar. Sci. Technol. 3 (1), 37–49. http://dx.doi.org/10.1007/BF01239805.

Kim, M.H., Kee, S.T., 1996. Flexible-membrane wave barrier. I: Analytic and numerical solutions. J. Waterw. Port Coast. Ocean Eng. 122 (1), 46–53. http://dx.doi.org/10.1061/(ASCE)0733-950X(1996)122:1(46).

Kim, M.W., Koo, W., Hong, S.Y., 2014. Numerical analysis of various artificial damping schemes in a three-dimensional numerical wave tank. Ocean Eng. 75, 165–173. http://dx.doi.org/10.1016/j.oceaneng.2013.10.012.

Koley, S., Sahoo, T., 2017. Oblique wave scattering by horizontal floating flexible porous membrane. Meccanica 52 (1–2), 125–138. http://dx.doi.org/10.1007/s11012-016-0407-1.

Lamas-Pardo, M., Iglesias, G., Carral, L., 2015. A review of very large floating structures (VLFS) for coastal and offshore uses. Ocean Eng. 109, 677–690. http://dx.doi.org/10.1016/j.oceaneng.2015.09.012.

Lo, E.Y.M., 2000. Performance of a flexible membrane wave barrier of a finite vertical extent. Coast. Eng. J. 42 (2), 237–251. http://dx.doi.org/10.1142/S0578563400000110.

Longuet-Higgins, M.S., 1977. The mean forces exerted by waves on floating or submerged bodies with applications to sand bars and wave power machines. Proc. R. Soc. A 352 (1671), 463–480. http://dx.doi.org/10.1098/rspa.1977.0011.

Loukogeorgaki, E., Michailides, C., Angelides, D.C., 2012. Hydroelastic analysis of a flexible mat-shaped floating breakwater under oblique wave action. J. Fluids Struct. 31, 103–124. http://dx.doi.org/10.1016/j.jfluidstructs.2012.02.011.

Ma, C., Iijima, K., Oka, M., 2020. Nonlinear waves in a floating thin elastic plate, predicted by a coupled SPH and FEM simulation and by an analytical solution. Ocean Eng. 204, 107243. http://dx.doi.org/10.1016/j.oceaneng.2020.107243.

Mansard, E., Funke, E., 1980. The measurement of incident and reflected spectra using a least squares method. In: Coastal Engineering 1980. 1 , New Yo, American Society of Civil Engineers, New York, NY, pp. 154–172. http://dx.doi.org/10.1061/9780872622647.008.

Mendoza, N., Boren, B., Niffenegger, J., 2023. Distributed embedded energy converter technologies for marine renewable energy (A technical report). Tech. Rep. NREL/TP–5700-85158, 1997371, MainId:85931, National Renewable Energy Laboratory (NREL), Golden, CO (United States), http://dx.doi.org/10.2172/1997371, URL https://www.osti.gov/servlets/purl/1997371/.

Michele, S., Buriani, F., Renzi, E., van Rooij, M., Jayawardhana, B., Vakis, A.I., 2020. Wave energy extraction by flexible floaters. Energies 13 (23), 6167. http://dx.doi.org/10.3390/en13236167, Number: 23 Publisher: Multidisciplinary Digital Publishing Institute.

Mohapatra, S., Guedes Soares, C., 2022. 3D hydroelastic modelling of fluid–structure interactions of porous flexible structures. J. Fluids Struct. 112, 103588. http://dx.doi.org/10.1016/j.jfluidstructs.2022.103588.

Moretti, G., Rizzello, G., Fontana, M., Seelecke, S., 2022. High-frequency voltage-driven vibrations in dielectric elastomer membranes. Mech. Syst. Signal Process. 168, 108677. http://dx.doi.org/10.1016/j.ymssp.2021.108677.

Ocean Sun, n.d. Ocean Sun: A bold solution to our global energy needs. URL https://oceansun.no/.

Ohmatsu, S., 2005. Overview: Research on wave loading and responses of VLFS. Mar. Struct. 18 (2), 149–168. http://dx.doi.org/10.1016/j.marstruc.2005.07.004.

Schreier, S., Jacobi, G., 2021. Experimental investigation of wave interaction with a thin floating sheet. Int. J. Offshore Polar Eng. 31 (4), 435–444. http://dx.doi.org/10.17736/ijope.2021.mk76.

Sheng, J., Chen, H., Liu, L., Zhang, J., Wang, Y., Jia, S., 2013. Dynamic electromechanical performance of viscoelastic dielectric elastomers. J. Appl. Phys. 114 (13), 1–8. http://dx.doi.org/10.1063/1.4823861.

Sree, D.K., Law, A.W.-K., Pang, D.S.C., Tan, S.T., Wang, C.L., Kew, J.H., Seow, W.K., Lim, V.H., 2022. Fluid-structural analysis of modular floating solar farms under wave motion. Sol. Energy 233, 161–181. http://dx.doi.org/10.1016/j.solener.2022.01.017, URL https://linkinghub.elsevier.com/retrieve/pii/S0038092X22000202.

Sree, D.K., Mandal, S., Law, A.W.-K., 2021. Surface wave interactions with submerged horizontal viscoelastic sheets. Appl. Ocean Res. 107, 102483. http://dx.doi.org/10.1016/j.apor.2020.102483.

Suresh Kumar, P., Manam, S., Sahoo, T., 2007. Wave scattering by flexible porous vertical membrane barrier in a two-layer fluid. J. Fluids Struct. 23 (4), 633–647. http://dx.doi.org/10.1016/j.jfluidstructs.2006.10.011.

Taylor, R., Ohkusu, M., 2000. Green functions for hydroelastic analysis of vibrating free–free beams and plates. Appl. Ocean Res. 22 (5), 295–314. http://dx.doi.org/10.1016/S0141-1187(00)00018-3.

Trivedi, K., Koley, S., 2022. Modeling the viscoelasticity of floating membrane in water waves. Mater. Today: Proc. http://dx.doi.org/10.1016/j.matpr.2022.07.047, S2214785322046454.

Verdugo, F., Badia, S., 2022. The software design of Gridap: A Finite Element package based on the Julia JIT compiler. Comput. Phys. Comm. 276, 108341. http://dx.doi.org/10.1016/j.cpc.2022.108341.

Vo, T.T.E., Ko, H., Huh, J., Park, N., 2021. Overview of possibilities of solar floating photovoltaic systems in the OffShore industry. Energies 14 (21), 6988. http://dx.doi.org/10.3390/en14216988.

Watanabe, E., Utsunomiya, T., Wang, C., 2004. Hydroelastic analysis of pontoon-type VLFS: a literature survey. Eng. Struct. 26 (2), 245–256. http://dx.doi.org/10.1016/j.engstruct.2003.10.001.

Williams, A.N., 1996. Floating membrane breakwater. J. Offshore Mech. Arct. Eng. 118 (1), 46–52. http://dx.doi.org/10.1115/1.2828800.

Xu, P., Wellens, P.R., 2022. Fully nonlinear hydroelastic modeling and analytic solution of large-scale floating photovoltaics in waves. J. Fluids Struct. 109, 103446. http://dx.doi.org/10.1016/j.jfluidstructs.2021.103446.

Zhang, M., Schreier, S., 2022. Review of wave interaction with continuous flexible floating structures. Ocean Eng. 264, 112404. http://dx.doi.org/10.1016/j.oceaneng.2022.112404.